2-2016

# Measuring the Seeds of Ion Outflow: Auroral Sounding Rocket Observations of Low-Altitude Ion Heating and Circulation

P. A. Fernandes
*Los Alamos National Labratory*, pfernandes@lanl.gov

K. A. Lynch
*Dartmouth College*

M. Zettergren
*Embry-Riddle Aeronautical University*, zettergm@erau.edu

D. L. Hampton
*University of Alaska, Fairbanks*

T. A. Bekkeng
*University of Oslo*

*See next page for additional authors*

AGU PUBLICATIONS

JGR

Journal of Geophysical Research: Space Physics

RESEARCH ARTICLE
10.1002/2015JA021536

# Measuring the seeds of ion outflow: Auroral sounding rocket observations of low-altitude ion heating and circulation

**P. A. Fernandes[1,2], K. A. Lynch[1], M. Zettergren[3], D. L. Hampton[4], T. A. Bekkeng[5], I. J. Cohen[6,7], M. Conde[4], L. E. Fisher[1], P. Horak[1], M. R. Lessard[6], R. J. Miceli[7,8], R. G. Michell[9,10], J. Moen[5], and S. P. Powell[11]**

[1]Department of Physics and Astronomy, Dartmouth College, Hanover, New Hampshire, USA, [2]Now at ISR-1 Space Science and Applications, Los Alamos National Laboratory, Los Alamos, New Mexico, USA, [3]Physical Sciences Department, Embry-Riddle Aeronautical University, Daytona Beach, Florida, USA, [4]Geophysical Institute, University of Alaska Fairbanks, Fairbanks, Alaska, USA, [5]Department of Physics, University of Oslo, Oslo, Norway, [6]Space Science Center, University of New Hampshire, Durham, New Hampshire, USA, [7]Now at The Johns Hopkins University Applied Physics Laboratory, Laurel, Maryland, USA, [8]Earth and Atmospheric Sciences, Cornell University, Ithaca, New York, USA, [9]Department of Astronomy, University of Maryland, College Park, Maryland, USA, [10]NASA Goddard Space Flight Center, Greenbelt, Maryland, USA, [11]Electrical and Computer Engineering Department, Cornell University, Ithaca, New York, USA

**Key Points:**
- In situ observations of low-altitude fine-scale structure and plasma circulation
- Wave-particle interactions heat ionosphere at altitudes below 325 km
- In situ observations of upflows in an auroral arc with downflows poleward of arc

**Correspondence to:**
P. A. Fernandes,
pfernandes@lanl.gov

**Citation:**
Fernandes, P. A., et al. (2016), Measuring the seeds of ion outflow: Auroral sounding rocket observations of low-altitude ion heating and circulation, *J. Geophys. Res. Space Physics*, *121*, 1587–1607, doi:10.1002/2015JA021536.

Received 3 JUN 2015
Accepted 15 JAN 2016
Accepted article online 25 JAN 2016
Published online 8 FEB 2016



**Abstract** We present an analysis of in situ measurements from the MICA (Magnetosphere-Ionosphere Coupling in the Alfvén Resonator) nightside auroral sounding rocket with comparisons to a multifluid ionospheric model. MICA made observations at altitudes below 325 km of the thermal ion kinetic particle distributions that are the origins of ion outflow. Late flight, in the vicinity of an auroral arc, we observe frictional processes controlling the ion temperature. Upflow of these cold ions is attributed to either the ambipolar field resulting from the heated electrons or possibly to ion-neutral collisions. We measure $\vec{E} \times \vec{B}$ convection away from the arc (poleward) and downflows of hundreds of m $s^{-1}$ poleward of this arc, indicating small-scale low-altitude plasma circulation. In the early flight we observe DC electromagnetic Poynting flux and associated ELF wave activity influencing the thermal ion temperature in regions of Alfvénic aurora. We observe enhanced, anisotropic ion temperatures which we conjecture are caused by transverse heating by wave-particle interactions (WPI) even at these low altitudes. Throughout this region we observe several hundred m $s^{-1}$ upflow of the bulk thermal ions colocated with WPI; however, the mirror force is negligible at these low energies; thus, the upflow is attributed to ambipolar fields (or possibly neutral upwelling drivers). The low-altitude MICA observations serve to inform future ionospheric modeling and simulations of (a) the need to consider the effects of heating by WPI at altitudes lower than previously considered viable and (b) the occurrence of structured and localized upflows/downflows below where higher-altitude heating rocesses are expected.

## 1. Introduction

In this paper we present a case study of the thermal ionospheric ion particle distributions that are the seeds of high-latitude ion outflow to the magnetosphere. Energization at low ionospheric altitudes results in bulk heating and transverse acceleration of the ions, which are eventually accelerated upward by the enhanced parallel pressure gradient and/or the mirror force, starting upflow and leading to the outflow process (see reviews by *André and Yau* [1997] and *Horwitz and Moore* [1997], and references within). These outflows have been well measured at higher altitudes by particle instruments, in the form of ion conics, including measurements at satellite altitudes [*Hoffman*, 1970; *Shelley et al.*, 1972; *Strangeway et al.*, 2005; *Nilsson et al.*, 2006] and by high-altitude sounding rockets [*Arnoldy et al.*, 1996; *Kintner et al.*, 1996; *Lynch et al.*, 2007] where the wave-particle interactions (WPI) have transversely accelerated these particles well beyond typical thermal energies. Generally speaking, it has been thought that transverse heating by WPI occurs at a minimum altitude of approximately 500 km on the nightside [*Whalen et al.*, 1978; *Yau et al.*, 1983; *Arnoldy et al.*, 1992]. Many investigations have shown that the outflow of oxygen into the magnetosphere has a profound effect on magnetospheric dynamics [*Kronberg et al.*, 2014, and references therein], such as the generation of magnetosphere sawtooth oscillations by ionospheric $O^+$ outflow [*Brambles et al.*, 2011] and changes in wave frequencies in ion cyclotron waves [*Lessard et al.*, 2015].

The mechanisms responsible for ion upflow/outflow are well documented in the literature. The two fundamental plasma physics mechanisms for initiating heating and/or upflow, both present in this case study, are frictional heating and heating by soft electron precipitation (older ground-based observation literature traditionally identifies these mechanisms as Type 1 and Type 2 heating, respectively [*Wahlund et al.*, 1992]). Frictional heating is caused by collisions between ions and neutrals given a relative drift between the two species and results in direct heating of the ions. This relative drift is typically produced by an electric field causing the ions to $\vec{E} \times \vec{B}$ convect through the neutral atmosphere [*Loranc et al.*, 1991; *Wahlund et al.*, 1992]. In this sounding rocket case study we do not have the instrumentation to measure perpendicular currents; therefore, we refer to the process of heating from ion-neutral collisions driven by convection as the more generalized expression "frictional heating," as opposed to Joule heating which results from currents driven by an electric field [*Vasyliunas and Song*, 2005]. (For an interesting theoretical comparison of frictional versus Joule heating, see *Brekke and Kamide* [1996].)

Theoretical and observational investigations correlate the degree of anisotropy ($T_\perp > T_\parallel$) at a given altitude with the strength of the electric field [*Perraut et al.*, 1984; *Glatthor and Hernández*, 1990; *Blelly et al.*, 2010; *Zettergren et al.*, 2011]. Conversely, heating by soft precipitation does not directly heat the thermal ions. Electron precipitation heats the ambient ionospheric electrons, which thermally expand upward where the ionospheric density is lower. This upward expansion creates an ambipolar electric field that accelerates the ions upward, initiating the upflow process [e.g., *Whitteker*, 1977; *Seo et al.*, 1997]. Additionally, recent observational and modeling studies have begun to stress the importance of neutral upwelling colocated with, and perhaps as a seed process for, ion upflow and outflow [*Lühr et al.*, 2004; *Schlegel et al.*, 2005; *Demars and Schunk*, 2007; *Sadler et al.*, 2012]. The MICA mission did not carry neutral instrumentation, so we cannot evaluate that contribution for this case study event, but we expect that it should play a role in these processes.

Soft electron precipitation is the primary driver of Type 2 ion upflow. Analysis by *Moen et al.* [2004] and *Skjæveland et al.* [2011] show a correlation between dayside episodic bursts of soft electron precipitation (poleward moving auroral forms) and ion upflows. Auroral fields lines with soft precipitation often carry wave power at Alfvén frequencies [e.g., *Chaston et al.*, 2002]. These Alfvén waves can be a source for wave-particle interactions through a nonlinear wave-breaking process that results in packets of broadband extremely low frequency (BBELF) emission [*Seyler et al.*, 1998]. Acceleration from wave-particle interactions results from a resonance between the plasma wave frequency and the ion gyrofrequency [*Chang and Coppi*, 1981]. This produces transverse acceleration of the ions, which manifests as a temperature anisotropy. The transversely accelerated ions are then accelerated upward by the mirror force [*Singh and Schunk*, 1984; *André et al.*, 1988; *Chang et al.*, 1986]. Ion acceleration may also be driven by Alfvén waves at altitudes above the aurora [*Lysak*, 1986; *Li and Temerin*, 1993; *Stasiewicz et al.*, 2000; *Chaston et al.*, 2004; *Singh et al.*, 2007; *Seyler and Liu*, 2007]. At these higher altitudes, wave heating from wave-particle interactions can further energize the upwelled ions, providing them sufficient energy to escape Earth's gravitational pull and escape to the magnetosphere [*Strangeway et al.*, 2005].

At the low altitudes of this case study, collisions play a critical role in the local ionospheric dynamics. When the ion-neutral collision frequency approaches the ion gyrofrequency, the emission of BBELF electrostatic ion cyclotron waves is suppressed [*Koepke et al.*, 1998]. When the ion-neutral collision frequency is comparable to or larger than the ion gyrofrequency, a collision occurs before the ion has sufficient time to complete a single gyration. For an anisotropic distribution of ions, these collisions will destroy the anisotropy and the distribution will revert toward a steady state isotropic Maxwellian distribution [*St-Maurice and Schunk*, 1979].

In situ measurements of ion distributions at the low altitudes where upflow/outflow processes are seeded are difficult because the observed distribution functions are dominated by flow, ram, and sheath effects. *Heelis and Hanson* [1998] discuss using a retarding potential analyzer (RPA) and an ion drift meter to measure low-energy plasma from an orbiting spacecraft. A more generalized review of low-energy plasma measurement techniques is given by *Moore et al.* [1998]. *Knudsen et al.* [1998a, 2003] and *Burchill* [2003] discuss several variations of a low-energy charged particle distribution imager used for measuring thermal ion distribution functions from satellites [*Knudsen et al.*, 1994, 1998b] and sounding rockets [*Burchill et al.*, 2004, 2010]. The analysis we present here from the MICA campaign augments this previous work by making these difficult measurements of thermal ion distribution functions at altitudes significantly lower than, and scales significantly smaller than, many of those previously presented.

Remote sensing using ground-based measurements can circumvent the difficulties associated with in situ measurements of thermal plasma, but these observations have their own limitations. Ground-based radar measurements of the high-latitude ionosphere commonly observe low-altitude (<1000 km) ion energization and upflow [*Wahlund and Opgenoorth*, 1989; *Forme et al.*, 1995; *Ogawa et al.*, 2009]. However, ground-based radar measurements such as those by PFISR (Poker Flat Incoherent Scatter Radar) integrate over a large horizontal pixel area (~10 km × 10 km per beam) at a range of 200 km. Beam-to-beam spacing is typically many tens of km in the *F* region (for the 15-beam pattern used on MICA) with integration times of tens of seconds to several minutes (M. Nicolls, personal communication, 2015). The combination of large pixel volume and long integration time makes these radar measurements incapable of resolving the fine-scale structures in the thermal ionosphere observed in situ by MICA. Additionally, because PFISR measures line-of-sight temperature, it is unable to distinguish between perpendicular and parallel heating within the observed volume containing the MICA trajectory (though this measurement within a common volume would be possible with multistatic measurements). Thus, the relationship between specific fine-scale processes and their net statistical aggregate effects remains an open question.

Many challenges impede proper analysis of in situ thermal ion distribution function data. In the low-energy regime, the response of the instrument varies from the ideal because the measured thermal ion population is very sensitive to the presence of the instrument. The plasma is distorted in the frame of the instrument because of plasma flows, payload ram, and acceleration through the sheath that forms around the spacecraft. The energies associated with these processes (a few eV) are large compared to the thermal energy (less than 0.5 eV). Extracting information about ion distribution function parameters from measurements of the thermal plasma distribution function requires accounting for all of these plasma processes and the nonideal response of the instrument in the low-energy regime. These techniques are essential to understanding the origin of the upflow/outflow process, in particular the details of the distribution functions and possible circulation patterns of the thermal ions at auroral field line foot points.

In this paper we describe the low-altitude in situ measurements of the thermal ion particle distributions from the MICA nightside auroral sounding rocket with comparisons to the multifluid ionospheric model of *Zettergren and Semeter* [2012]. The techniques and observations in this study differ from previous ionospheric observations of the origins of ion outflow in several ways. The ion measurements are derived from a novel forward-modeling technique that allows us to extract ion temperature and parallel flows from the saturated measurement of the 2-D thermal ion distribution. This new technique is an extension of previous work in which forward-modeling images of the in situ measured thermal ion distribution function were used to extract geophysical quantities [*Burchill*, 2003; *Knudsen et al.*, 2003; *Burchill et al.*, 2004]. Our observations of the processes that seed ion upflow/outflow are at altitudes below 325 km. Specifically, the observations of processes influenced by WPI, and the occurrence of structured and localized upflows and downflows on a Type 2 field line are at altitudes below where higher-altitude heating processes are expected. These low-altitude observations inform future ionospheric observations, modeling, and simulations of the need to consider heating by WPI and structured parallel flows at altitudes lower than previously considered viable.

In sections 2.1 and 2.2 we describe the MICA mission and event. In sections 2.3 and 3.1 we present the MICA in situ and ground-based data. In sections 3.2 and 3.3 we analyze the thermal ion data using a forward-modeling technique. In sections 4.1 and 4.2 we present and discuss the results of our analysis. In section 4.3 we compare the in situ data to a multifluid ionospheric model. In section 5 we present our conclusions.

## 2. Observations

### 2.1. MICA Flight Overview

The details of the MICA (Magnetosphere-Ionosphere Coupling in the Alfvén Resonator) nightside auroral sounding rocket mission have been presented in *Zettergren et al.* [2014] and *Lynch et al.* [2015]. In this section we present those details pertinent to the analysis of the thermal ion data.

MICA (NASA 36.273) launched from the Poker Flat Research Range in central Alaska on 19 February 2012 at 05:41:06.745 UT (or 18 February 2012 at 18:11:06.745 MLT). It reached an apogee of 325 km at $T + 297.5$ s. The MICA payload traversed two discrete, localized arcs in the wake of a westward traveling surge. Here we focus on the behavior of thermal ions in and poleward of the two small auroral arc structures.

### 2.2. Instrumentation

The MICA campaign consisted of the science payload and a suite of ground-based instruments. The MICA science payload split into a main payload and a subpayload. The spin axes of both payloads were aligned to the local magnetic field within fewer than 4° throughout the flight. The final spin rate of the main payload was approximately 0.6 Hz, and the final spin rate of the subpayload was approximately 0.4 Hz. The subpayload separated from the main payload at $T+98$ s at a separation rate of 1.25 m s$^{-1}$. The subpayload carried a thermal electron retarding potential analyzer (ERPA) [*Frederick-Frost et al.*, 2007], a Cornell University GPS Autonomous Receiver (COUGAR) [*Powell et al.*, 2002], and the Cornell Wire Boom Yo-yo (COWBOY) electric field instrument [*Lundberg et al.*, 2012a, 2012b]. As described by *Lundberg et al.* [2012b], the COWBOY instrument consists of a pair of crossed 12.14 m dipole antennas. Potential difference is measured between the 4.45 cm spheres at the end of each coaxial wire boom, as well as between each sphere and the payload skin. The antennas were connected to two wave receivers: one measuring from DC to 500 Hz at a sample rate of 1 kHz and one measuring from 20 Hz to 20 kHz. One sphere pair was equipped with an HF snapshot receiver that took 4096 samples at 4.8 MHz once every 10 ms. All data presented in this analysis were acquired with the DC (0–500 Hz) plasma wave receiver.

The main payload carried a Billingsley fluxgate magnetometer (Billingsley TFM100G2). As described by *Lynch et al.* [2015], the magnetometer acquired data at 1 kHz; these magnetic field data are despun from the payload reference frame using a rigid body motion model of the payload dynamics [*Horak*, 2014]. The despun data are differenced from an IGRF (International Geomagnetic Reference Field) model to find the deflections caused by auroral currents. The data are smoothed but not band-pass filtered, in order to retain the proper phase of the resulting signals.

Other instruments on the main payload include a second ERPA, a second GPS receiver, a suite of five thermal ion retarding potential analyzers (PIPs or Petite Ion Probes), a toroidal electrostatic analyzer for measuring precipitating electrons (the Bagel), a multineedle Langmuir probe (mNLP) [*Moen et al.*, 2012; *Bekkeng et al.*, 2010; *Jacobsen et al.*, 2010], and a top-hat thermal ion electrostatic analyzer (HEEPS-Thermal, HT ). The results we present in this paper focus on the analysis of the thermal ion data from the HT (HEEPS-Thermal or hemispherical energetic electrostatic particle spectrometer-thermal) instrument.

The HT instrument is based on a traditional stretched top-hat electrostatic analyzer detector design [*Carlson et al.*, 1983; *Young et al.*, 1988]. The physical parameters of the HT (using the definitions given by *Young et al.* [1988]) are the following: minor radius $R_1 = 1.778$ cm; major radius $R_2 = 1.905$ cm; stretch radius $R_A = 6.096 \times 10^{-2}$ cm; and geometric factor (per pixel) $G = 5.07 \times 10^{-5}$ cm$^2$ sr. The HT measures the thermal ion phase space distribution $f(v_\perp, v_\parallel)$ over a nominal energy range of 0.019–73 eV at a 2 kHz sample rate with a 128 ms energy sweep period. The planar field of view (FOV) defined by the aperture is approximately 270° × 5°. The HT is mounted such that the spin axis is within the planar FOV; thus, the instrument was flown with the background geomagnetic field $\vec{B}_0$ located in the planar field of view (fewer than 4° separate the magnetic field vector and the FOV plane). Payload spin sweeps the FOV plane through all directions perpendicular to $\vec{B}_0$ allowing for measurement of the full 3-D distribution function. Detailed analysis of the HT thermal ion data is discussed in section 3.

The in situ measurements are interpreted in the context of a ground-based array of sensors including imagers and radar. PFISR was run in a 15-beam mode allowing observations of plasma density and large-scale electric fields. (See *Zettergren et al.* [2014] for a detailed description of the PFISR experiment and data from the MICA campaign.) A Scanning Doppler Imager (SDI, a Fabry-Perot interferometer) at Poker Flat monitored *E* and *F* region neutral winds and temperatures [*Conde and Smith*, 1998; *Anderson et al.*, 2012a, 2012b]. A digital all-sky imager was operating at Poker Flat, filtered for the oxygen red and green-line emissions (630.0 and 557.7 nm), and in particular the $N_2^+$ first negative emission at 427.8 nm, cycling through the three filters on a 12.5 s cadence. A medium-field (47° field of view) imager, looking up the local magnetic field line, filtered for the $N_2^+$ first negative emission at 427.8 nm and operating at 16.4 Hz, was operating under the foot point of the payload apogee at Venetie, Alaska.

### 2.3. Observations

Figure 1 shows a keogram display of the auroral event and the MICA payload traversal through the two auroral arcs. This keogram, generated from the data acquired by the Venetie medium-field imager, is cut along the line of the payload trajectory and displays electron energy flux calculated using the conversion factors of *Rees*

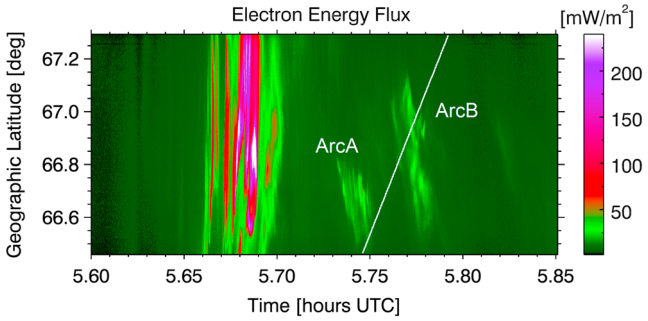


**Figure 1.** Keogram showing an overview of the MICA event; the white line represents the MICA payload trajectory. The keogram is cut along the payload trajectory from the medium-field imager, which was located at Venetie (foot point of apogee) and centered on the local magnetic field line. The keogram shows electron energy flux calculated from the optical data.

*and Luckey* [1974] and *Strickland et al.* [1989]. This keogram shows the time history of each point along the trajectory (the diagonal white line indicates the MICA payload trajectory as a function of time).

Early in the evening (before this keogram), a quiet evening arc crossed Alaska. Magnetometer measurements from the GOES satellite and camera data from the THEMIS camera array indicated the onset of a substorm that launched a westward traveling surge toward Alaska. Minutes before the MICA launch, this westward traveling surge crossed into the field of view of the Poker Flat and Fort Yukon all-sky imagers. This activity is seen in the Figure 1 keogram from 5.66 to 5.70 UT. The rocket was launched into the wake of this surge. As shown in the keogram the MICA payload transited the first arc, labeled ArcA, at 5.75 UT (flight time $T$ + 233 s). A second crossing, labeled ArcB, occurs at 5.77 UT ($T$ + 286 s).

Figure 2 shows an overview of the in situ and ground-based observations during the MICA flight. The payload transits ArcA from $T$ + 233–241 s, defined by the optical data (Figure 2a); ArcB extends from $T$ + 286–337 s, defined by the current sheet signature in the magnetic field data (Figure 2c). Figure 2a shows the payload altitude and the auroral intensity at the magnetic foot point of the payload from the Venetie medium-field imager. This imager is filtered for the 427.8 nm blue line with an assumed peak altitude of 110 km. Figure 2b is the DC-coupled electric field (0–500 Hz) rotated into a geomagnetic coordinate system. Figure 2c is the DC-coupled magnetic field deflection (differenced from the IGRF model) rotated into the same geomagnetic coordinate system. Note that the coordinate system used is geomagnetic-north (blue), geomagnetic-east (red), geomagnetic-down, so the magnetic field data, the DC Poynting flux (presented later), and field-aligned currents (FAC) are positive pointing downward toward Earth's surface for this Northern Hemisphere mission. The prominent feature in the magnetic field data is the large upward current sheet observed from $T$+286–337 s as the payload moves northward through ArcB. Figure 2d is the large-scale field-aligned current calculated from the curl of the magnetic deflection vector (calculation detailed in *Lynch et al.* [2015]).

The electric and magnetic field data presented in Figures 2b and 2c are used to calculate the DC electromagnetic Poynting flux presented later in the analysis (section 4). This DC Poynting flux is the cross product of the DC electric field (0–500 Hz) and the magnetic field deflection. Because both quantities are sampled at 1 kHz, the calculated Poynting flux covers the frequency range 0–500 Hz and thus includes power from DC and Alfvénic sources.

Figure 2e shows the plasma density (from mNLP) and electron temperature (from subpayload ERPA). The largest-scale features of the density profile are governed by altitude, with $F$ region peaks observed at $T$+190 s and $T$ + 425 s. A density cavity is observed from approximately $T$ + 200–375 s; as discussed by *Zettergren et al.* [2014] this cavity is consistent with a hysteresis effect in the $F$ region driven by the strong electric fields preceding the recent passage of the westward traveling surge. Their modeling shows that the generation and fast recombination of heavy molecular ions can leave density gaps in the $F$ region for tens of minutes. Furthermore, their analysis implies that these $F$ region density cavities may persist in spite of the surge ionization source enhancement in the $E$ region. Figure 2f shows the ion temperatures parallel and perpendicular to $\vec{B}_0$, with a temperature anisotropy of $T_\perp/T_\parallel = 1.3$ for the first half of the flight ($T$ + 163–285 s) and a nearly isotropic temperature for the second half. Figure 2g shows the bulk parallel motion of the thermal ions for the previously described temperature anisotropy, with positive along $\vec{B}_0$ (positive flows are downflows).

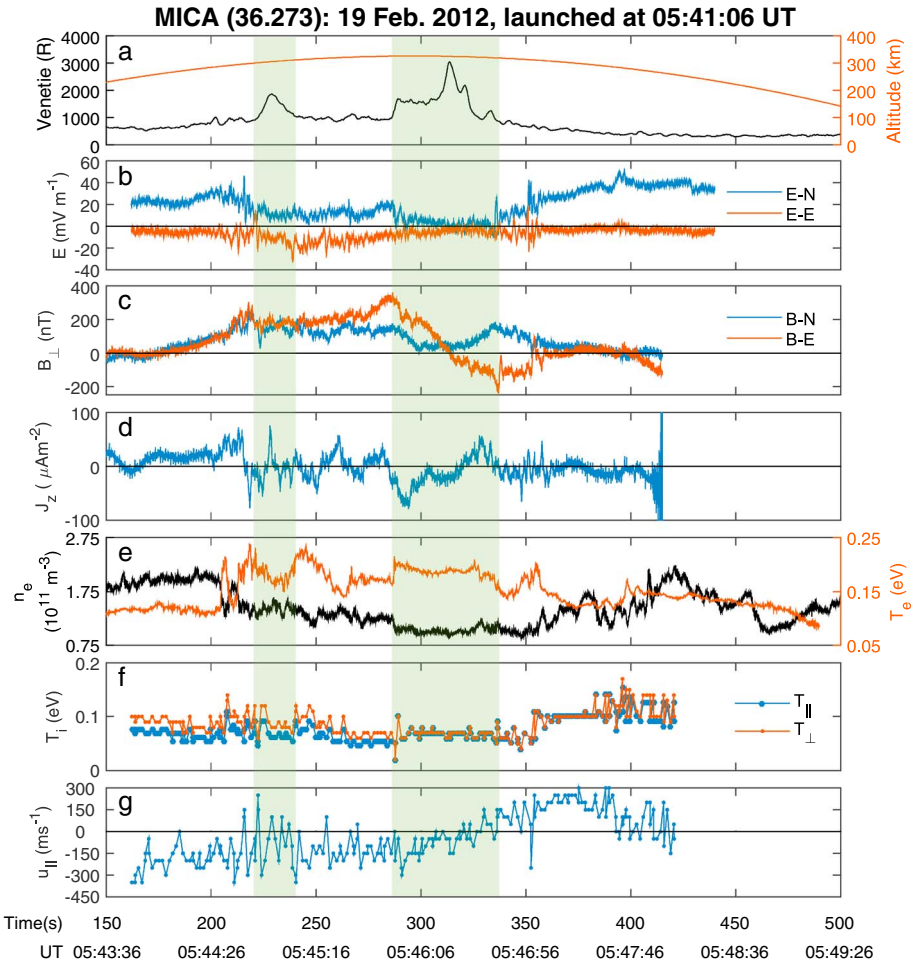


**Figure 2.** MICA in situ and camera data. The highlighted regions are ArcA ($T + 233 - 241$ s) and ArcB ($T + 286 - 337$ s). The figure shows (a) intensity from the Venetie medium-field imager (black) and payload altitude (red); (b) electric field and (c) magnetic field measurements in geomagnetic north (blue) and east (red) coordinates; (d) field-aligned current where positive is along $\vec{B}_0$; (e) electron density (black) and electron temperature (red); (f) ion temperature parallel (blue) and perpendicular (red) to $\vec{B}_0$; and (g) parallel motion of thermal ions, where positive is downflow (parallel to $\vec{B}_0$) and negative is upflow.

The focus of this manuscript is the in situ thermal ion data presented in Figures 2f and 2g. These geophysical parameters result from analysis using a forward model that generates ion images from a simulation of the velocity distribution function. This forward model is driven by the in situ measurements of the plasma density $n$, electric fields $\vec{E}$, and the spacecraft potential $\Phi_{sc}$. The geophysical parameters that result from our analysis are the gyrotropic thermal ion temperature, $T_\perp$ and $T_\parallel$, and the bulk parallel ion flow velocity, $u_\parallel$. The analysis technique is described in section 3.

## 3. Analysis

### 3.1. Thermal Ion Images

Analysis of the HT thermal ion data requires accounting for shifts and accelerations of the plasma as measured in the instrument frame. The energies associated with these processes are large compared to the thermal energy. The spacecraft is charged to several volts negative in the dark lower ionosphere [*Siddiqui et al.*, 2011], so the acceleration from the spacecraft potential dominates the energy response. We assume a thin-sheath spherically radial acceleration of thermal ions to the instrument aperture, a simplifying assumption that assumes the acceleration occurs in a region of zero thickness at the instrument aperture. As such, we limit our analysis to times when the instrument FOV plane is within 20° of the perpendicular ram vector (the component of the net flow perpendicular to the spin axis), because at these ram-facing times the sheath and ram acceleration vectors are nearly parallel, and the thin-sheath approximation is accurate. We explicitly account

for the $\vec{E} \times \vec{B}$ geophysical plasma flow and the ram (both measured quantities) as the payload travels through the flowing thermal plasma (at approximately 1 km $s^{-1}$, i.e., at speeds comparable to the ion thermal speed).

We have carefully excluded data that are contaminated by detector saturation. The region of uncontaminated data was estimated by reproducing the saturation with our flight spare detector in the Dartmouth ELEPHANT (Experimental Low Energy Plasma for Hemispherical Analyzer Nominal Testing) calibration chamber facility [*Frederick-Frost and Lynch*, 2007; *Gayetsky and Lynch*, 2011; *Siddiqui et al.*, 2011]. We found that saturation resulting in pitch angle imaging distortion occurs for count rates greater than 130 kHz. Considering then the MICA flight data, we continually monitor the count rate and corresponding saturation limit, retaining only the uncontaminated data. The saturation distorts the pitch angle imaging of the instrument in the energy bins corresponding to the core of the distribution, meaning that we are limited to analyzing the higher-energy tail of the distribution. The thermal ion data within this limited phase space window are analyzed by comparison with a 3-D Maxwellian representation of ionospheric thermal ions using a forward-modeling technique within the same limited phase space window.

### 3.2. 3-D Maxwellian Model

The analysis of the uncontaminated HT thermal ion data is conducted by comparison to a modeled 3-D Maxwellian representation of ionospheric thermal ions. As we will show later in section 4.1, collisionality at these altitudes results in plasmas that are generally quite close to thermal equilibrium, with anisotropies of only a few percent unless there are local drivers such as wave-particle interactions. This 3-D Maxwellian representation of the ionospheric thermal ion distribution function is given by

$$f(v_{\perp_1}, v_{\perp_2}, v_{\parallel}) = n\left(\frac{m_i}{2\pi k_B}\right)^{\frac{3}{2}}\left(\frac{1}{T_{\perp_1}T_{\perp_2}T_{\parallel}}\right)^{\frac{1}{2}} \exp\left\{\frac{-m_i(v_{\perp_1}-u_{\perp_1})^2}{2k_BT_{\perp_1}}+\frac{-m_i(v_{\perp_2}-u_{\perp_2})^2}{2k_BT_{\perp_2}}+\frac{-m_i(v_{\parallel}-u_{\parallel})^2}{2k_BT_{\parallel}}+e\Phi_{sc}\right\}. \quad (1)$$

The plasma density is $n$; $k_B$ is the Boltzmann constant; $m_i$ is the ion mass; $e$ is the fundamental electric charge; $T_{\parallel}$, $T_{\perp_1}$, $T_{\perp_2}$, $u_{\parallel}$, $u_{\perp_1}$, and $u_{\perp_2}$ are the temperatures and drift velocities, respectively, measured with respect to the magnetic field direction. The spacecraft potential $\Phi_{sc}$ is given by *Siddiqui et al.* [2011] as

$$\Phi_{sc} = -\frac{k_BT_e}{e}\ln\left(\sqrt{\frac{m_iT_e}{m_eT_i}}\right) - V_{ss} \quad (2)$$

where $m_e$ is the electron mass, $T_i$ is the (isotropic) ion temperature, $T_e$ is the electron temperature (from ERPA, Figure 2e), and $V_{ss}$ is the spacecraft sphere-to-skin voltage difference measured by the COWBOY. The first term represents the idealized float potential of a perfectly conducting sphere; the second term is the measured difference between such a sphere (the electric field probes) and the irregular nonideal spacecraft (this term is reported positive and thus serves to further decrease the spacecraft potential). This measurement is from the subpayload but provides a good representation of the main payload charging in the same nearby environment. For this calculation (equation (2)) we assume $T_i = T_e$ which is a small error within the argument of the natural logarithm.

We simplify equation (1) by treating the undisturbed plasma as gyrotropic; that is, $T_{\perp_1} = T_{\perp_2}$. Two examples of this bi-Maxwellian distribution are shown in Figure 3. The mass is assumed to be 100% $O^+$; this simplifying approximation is based on the results of *Zettergren et al.* [2010], which show the ionosphere composition to be 60–95% $O^+$ at 250 km and 95–99% $O^+$ at 300 km. Parameters in the forward model given by simultaneous time-dependent in situ measurements include the plasma density $n$ (from mNLP), the spacecraft potential $\Phi_{sc}$ (calculated from ERPA and COWBOY measurements), and perpendicular drift velocities $u_{\perp_1}$ and $u_{\perp_2}$ (geophysical plasma flow from COWBOY and plasma ram from GPS). The flow measurements (from the subpayload) have been despun into the geomagnetic reference frame, then spun up into the frame of the main payload. The remaining parameters (temperatures $T_{\parallel}$, $T_{\perp}$, and the parallel drift velocity $u_{\parallel}$) are adjusted until the modeled distribution matches the in situ measured distribution within the limited phase space window; this technique of adjusting the model to match the measurement is the "forward-modeling" technique. More specifically, we match the uncontaminated in situ data with the equivalent phase space density from the model for each time sample when the plasma net flow direction is within 20° of the HT planar FOV.

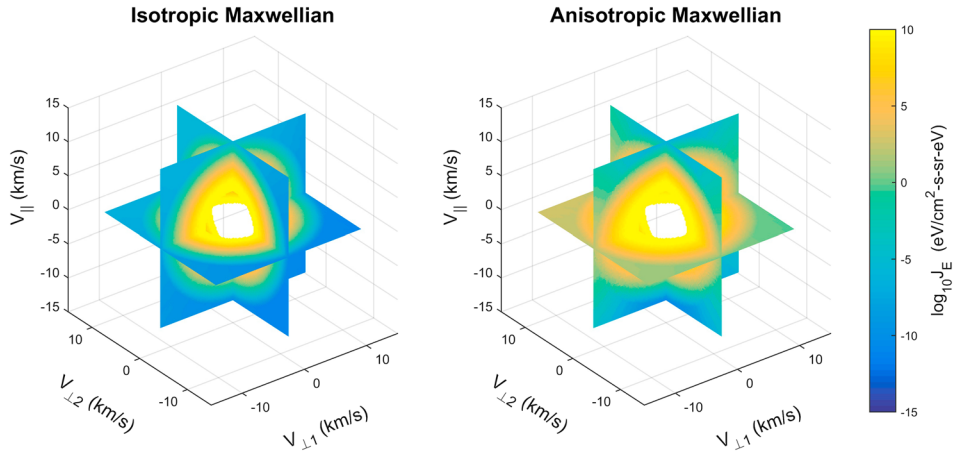


**Figure 3.** Two examples of the 3-D Maxwellian distribution function used in the forward model, for (left) isotropic and (right) anisotropic distributions. The anisotropic distribution is defined by $T_\perp / T_\parallel = 2.0$ with $T_{\perp_1} = T_{\perp_2} = T_\perp$. Both examples of the model use $T_\parallel = 0.21$ eV and include a 1.5 eV spacecraft potential, which manifests as a hole in the center of the distribution. These examples also include velocity drifts representing those from ram and geophysical flows, which appear as an offset of the distribution from origin. The velocity drifts used are the following: $u_\parallel = 500$ m s$^{-1}$; $u_{\perp_1} = -500$ m s$^{-1}$; $u_{\perp_2} = 0$ m s$^{-1}$.

### 3.3. Forward Model

The forward-modeling technique involves adjusting the fit parameters in the 3-D Maxwellian model (temperature and parallel drift velocity) until bulk parameters calculated from the model match the bulk parameters calculated from the in situ measured distribution function. We begin this analysis by assuming the simple case of an isotropic ion temperature ($T_\perp = T_\parallel$), though later we evaluate the impacts of anisotropy. In order to quantitatively compare model and measurement, we develop two intermediate data products: the weighted-average pitch angle (WAPA) and the net radial flux to the aperture (RFA). These data products are independent of each other, but they are both dependent on the desired geophysical parameters of ion temperature $T_i$ and parallel drift velocity $u_\parallel$.

The weighted-average pitch angle is given by

$$\mathrm{WAPA} = \frac{\sum_i \sum_j C_{ij}\, \alpha_i}{\sum_i \sum_j C_{ij}} \tag{3}$$

where $j$ is the index for summing over energy steps above the time-dependent saturation threshold, $i$ is the index for summing pitch angle bins over the range $[0, \pi]$, $C_{ij}$ is the count rate at pitch angle bin $i$ and energy step $j$, and $\alpha_i$ is the pitch angle of the particles associated with pitch angle bin $i$ as they enter the detector aperture. This WAPA is calculated both for the data and for the model, for a restricted window of phase space limited by the time-dependent saturation cutoff count rate of 130 kHz. For the model we use equation (3) to calculate the WAPA by converting the distribution function $f$ given by equation (1) into a count rate $C_{ij}$ using

$$C_{ij} = f_{ij} \frac{2GE_j^2}{m^2} \tag{4}$$

where $m$ is the mass, $G$ is the geometric factor of the instrument, and $E_j$ is the energy corresponding to energy bin $j$.

The ideal net radial flux to the payload, by Liouville's theorem, must be the same inside and outside the sheath, despite any defocusing effects caused by the sheath. In defining the net radial flux to the aperture we make the thin-sheath approximation in which we assume particle trajectories experience an instantaneous radial acceleration at the boundary of the zero-thickness sheath. As discussed in section 3.1 we mitigate sheath effects by limiting analysis to times when the ram vector is within 20° of the FOV plane. The net radial flux to the aperture is given by

$$\mathrm{RFA} = \sum_i \sum_j \frac{E_j}{2m^2} f_{ij}\, \Delta E_j\, \Delta\Omega_i \tag{5}$$

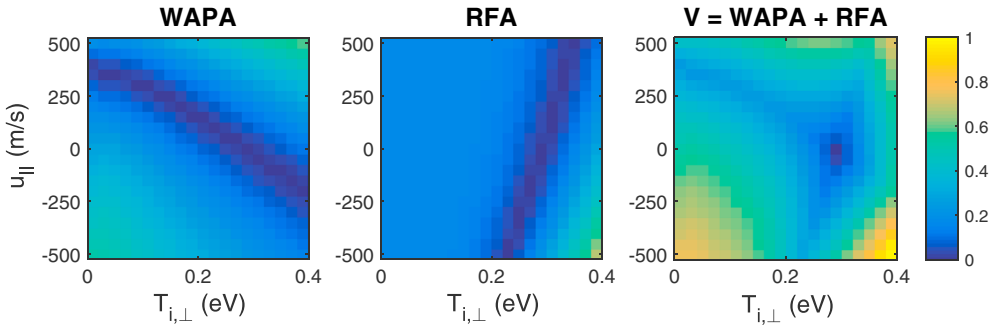


**Figure 4.** An illustrative example of the minimization technique used for comparing in situ data and the forward model. (left and middle) The intermediate data products weighted-average pitch angle (WAPA) and radial flux to the aperture (RFA) differenced from their data equivalents, for a single HT image at a given flight time $t$, as functions of $T_{i,\perp}$ and $u_{||}$. Specifically, these panels show the difference between the in situ data and the forward model for a series of parallel flow velocities and temperatures. (right) These intermediate data products are combined as shown, in which the resulting minimum yields the ordered pair ($T_{i,\perp}$, $u_{||}$) for the given time $t$. Color scales in all panels are normalized.

where $j$ is the index for summing over energy steps above the time-dependent saturation threshold, $i$ is the index for summing pitch angle bins over the range $[0, \pi]$, $E_j$ is the energy associated with each energy step $j$ of the detector, $\Delta E_j$ is the spacing of each energy step, $\Delta\Omega_i$ is angular spacing of the solid angle of acceptance, $m$ is the ion mass, and $f_{ij}$ is the distribution function given by equation (1). Like the WAPA, this RFA is calculated both for the data and for the model, for a restricted window of phase space limited by the time-dependent saturation cutoff count rate. Liouville's theorem is only strictly true for the full distribution; however, the comparison of in situ and modeled RFA above the saturation energy threshold gives reasonable results. To calculate the RFA from the in situ data, we convert the count rate $C_{ij}$ to the distribution function $f_{ij}$ using equation (4).

Recalling that intermediate quantities WAPA and RFA are independent of each other but are both dependent on $T_i$ and $u_{||}$, we calculate these intermediate quantities for only the uncontaminated phase space, which includes all energy bins above the step where the count rate at that time falls below the saturation cutoff of 130 kHz. Specifically, for each in situ thermal ion image at ram-looking sample times, we directly calculate the WAPA and RFA using only the uncontaminated phase space. At each given time, we then use the model to calculate the WAPA and RFA for the same uncontaminated phase space for a range of values of $T_i$ and $u_{||}$. For each ordered pair ($T_i$, $u_{||}$) we use a variation of the Lagrangian minimization technique to find the minimum difference between in situ measurement and model for both WAPA and log(RFA). Figure 4 shows an illustrative example of this differencing technique, showing the differenced WAPA, RFA, and the minimization of both intermediate data products. (For the specific data calculations in this analysis, log(RFA) was used.) Repeating this process for each valid thermal ion image results in a time series of $T_i$ and $u_{||}$, our resultant geophysical data products, shown in Figure 5.

Parts of the flight require accounting for possible temperature anisotropies in the thermal ion distribution. We define the temperature anisotropy as the ratio of the perpendicular temperature to the parallel temperature: $T_\perp/T_{||}$. The analysis for anisotropic populations is conducted as previously described with one caveat: a single value of anisotropy is first imposed, and then the minimization technique is applied to the two intermediate data products WAPA and log(RFA), resulting in time series of geophysical data products $T_\perp$ and $u_{||}$ for each anisotropy value. We then select the appropriate value for anisotropy based on the geophysical processes driving the ion temperature, as discussed in sections 4.1 and 4.2. Based on these selection criteria we use the geophysical data products $T_\perp$ and $u_{||}$ to quantify the state of the ionosphere during the MICA event.

## 4. Discussion and Comparison to Previous Observations

In order to analyze the thermal ion data we divide the flight into two distinct periods based on which local drivers are observed to control the thermal ion population. Referencing Figure 2, we split the flight into an early interval ($T$ + 163–285 s, includes ArcA) and a later interval ($T$ + 286–421 s, includes ArcB). Referencing Figure 6, during the later interval we will show that the DC electric fields are the primary controller of the thermal ion temperature, whereas in the early interval frictional heating is not sufficient to explain the

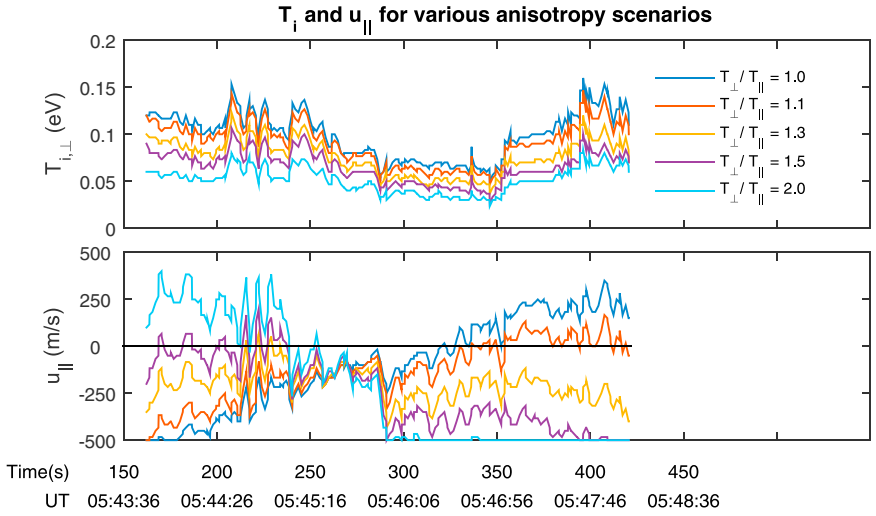


**Figure 5.** Time series of measured perpendicular ion temperature (top) and parallel ion velocity (bottom) for anisotropies ranging from $T_\perp/T_\parallel = 1.0-2.0$. For $T + 163-285$ s our analysis introduces an anisotropy ranging from 1.1–2.0. Upon entering ArcB at $T + 286$ s, until $T + 421$ s, our analysis indicates a nearly isotropic distribution with a maximum anisotropy of 1.08 (blue and red traces). Our analysis indicates that $T_i$ is insensitive and $u_\parallel$ is very sensitive to choice of anisotropy.

observed temperatures and level of anisotropy; thus, other mechanisms must be considered. Throughout the flight, ion upflows are observed but cannot be attributed to the mirror force at these low altitudes and energies. An example calculation of the mirror force for a 0.2 eV $O^+$ ion at 275 km indicates that the gravitational force is 17 times greater than the mirror force. Rather, the ion upflows likely result from heating of the ambient plasma population followed by an increase in the ion and/or electron scale height to reestablish equilibrium. At these low altitudes, an additional possibility is that neutrals are upwelling, and collisional and/or charge exchange processes between ions and neutrals are driving the ion upwelling.

### 4.1. Quasi-Static Frictional Processes: $T + 286-421$ s

This interval of the flight is defined by the payload entering ArcB and includes the traversal of the arc as well as the downward current region poleward of the arc. Figure 6 shows that the inflowing DC Poynting flux is very low inside and poleward of ArcB. This can be interpreted in two ways: precipitation enhancing the

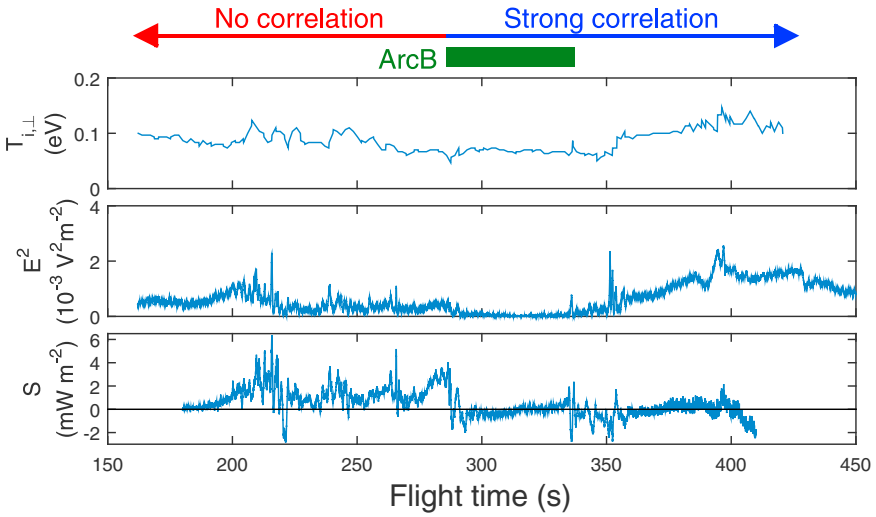


**Figure 6.** In situ measurements of (top) the ion temperature, (middle) electric field power from 16 to 80 Hz, and (bottom) calculated DC Poynting flux. ArcB is indicated at the top of the figure with the payload entering the arc at $T + 286$ s. Prior to entering the arc there is no significant correlation between $T_i$ and $E'^2$. Within ArcB and the poleward downward current region $T_i$ and $E'^2$ are strongly correlated, which we interpret as frictional heating driving the ion temperature.

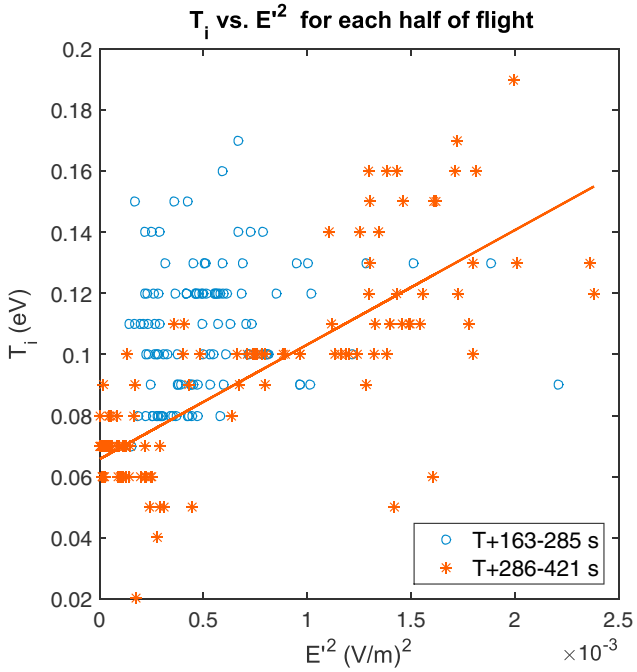


**Figure 7.** Relationship between in situ measurements of ion temperature and electric field $E'$, the effective electric field after accounting for the velocity of the neutrals. Solid/red markers are for $T + 286–421$ s including ArcB and the poleward downward current region. The correlation coefficient in this region is $R = 0.78$. Empty/blue markers are for times prior to $T + 286$ s and show no significant correlation ($R = 0.16$).

conductivity [*Reiff*, 1984] and reducing the ionospheric electric field [see *Marklund* [2009] and references within] or the conversion of electromagnetic energy to particle energy in the U-shaped potential structure inferred above ArcB [*Wygant et al.*, 2000; *Chaston et al.*, 2002; *Paschmann et al.*, 2003; *Dombeck et al.*, 2005]. The minimal inflowing DC Poynting flux, the absence of Alfvénic activity (an indirect source for ELF WPI) in the camera data, and the low ion temperatures (especially within ArcB) imply that there are no ELF wave-particle interactions in this region. (A lone exception occurs at $T + 350$ s, in which a brief burst of BBELF corresponds to a spike in the ion temperature, as seen in Figure 10; this localized downward current region is explored by *Lynch et al.* [2015].)

In regions with no WPI and moderate to strong DC electric fields, frictional heating is the primary driver of the thermal ion temperature [*Schunk and Nagy*, 2009; *Kelley*, 2009]. As shown in Figure 7, throughout this region we observe a strong correlation between the ion temperature $T_i$ and the DC electric field power $E'^2$, with the correlation coefficient (Pearson R) $R = 0.78$. However, this does not lead to significant upflow because $T_i$ is too low. We fit this relation using a linear least squares regression fitting technique; the resulting relationship is given by

$$T_i = T_n + 37.5E'^2 \tag{6}$$

where $T_i$ and $T_n$ are the ion and neutral temperatures in eV, and $E'$ is the effective electric field in V m$^{-1}$ after accounting for the velocity of the neutrals, given by $\vec{E}' = \vec{E} + \vec{u}_n \times \vec{B}$. The neutral velocity $\vec{u}_n$ used in this analysis is the average neutral wind velocity at 240 km altitude as measured by the ground-based SDI Fabry-Perot interferometer: approximately 150 m s$^{-1}$ N and 160 m s$^{-1}$ W. This neutral velocity is small relative to the ram (~1 km s$^{-1}$) but comparable to the electric field flow velocities. We obtain (from fitting to equation (6)) an estimated average neutral temperature of $T_n = 770 \pm 230$ K (or $0.066 \pm 0.020$ eV) over the altitude range 260–325 km. This is comparable to the neutral temperature reported by the ground-based SDI Fabry-Perot interferometer (approximately $930 \pm 50$ K at 250 km). Equation (6) is compared with theoretical results for regions with strong frictional heating and no WPI; comparing the slope (37.5 eV m$^2$ V$^{-2}$) with the theoretical predictions by *Schunk and Nagy* [2009] (28.4 eV m$^2$ V$^{-2}$) and *Zettergren et al.* [2011] (30.2 eV m$^2$ V$^{-2}$) shows basic agreement with theoretical predictions. The calculated dependence of $T_i$ on $E'^2$ in a region of strong frictional heating with no WPI serves as a metric to validate our forward-modeling ion data analysis technique despite the limitations of the data set.

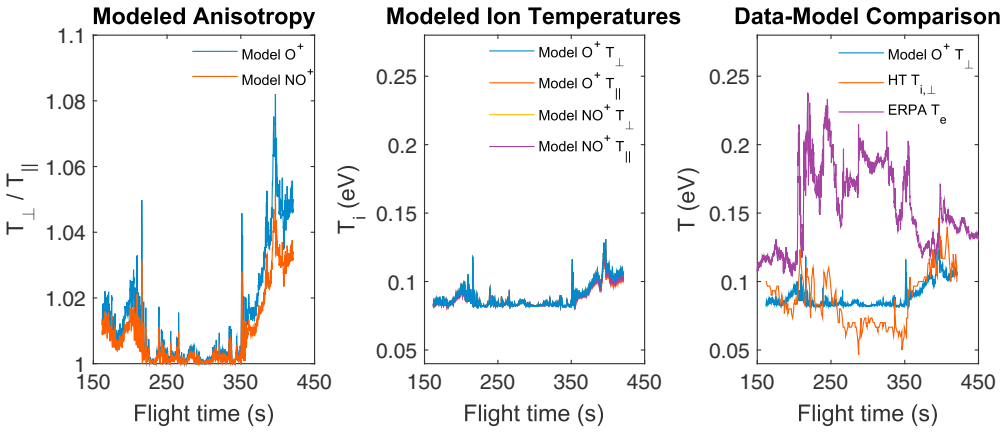


**Figure 8.** (left) Anisotropy generated by DC electric fields, calculated from the steady state solution to 13-moment energy and pressure tensor equations and applied to the MICA flight. (middle) The modeled perpendicular and parallel temperatures for $O^+$ and $NO^+$. (right) The comparison of modeled $O^+$ perpendicular temperature with ion and electron temperatures measured in situ.

These DC electric fields generate a temperature anisotropy that can be calculated from a steady state solution to 13-moment energy and pressure tensor equations [*Schunk*, 1977; *Blelly et al.*, 2010] which includes both ion-neutral and Coulomb collisions (ion-ion and ion-electron). The calculation is done first for a system of $O^+$ and then $NO^+$ ions. For executing this calculation we take DC electric field data, electron temperature data, and electron density data directly from the rocket measurements. Neutral densities have been taken from MSIS00, but the solar and geomagnetic activities have been adjusted to yield thermospheric temperatures consistent with the SDI ground-based measurements taken the night of the MICA flight. The DC electric field-driven anisotropy predicted by this mathematical model and applied to the specific case of MICA is shown in Figure 8. (Note that this steady state solution used to calculate anisotropy is distinct from the multifluid ionospheric model to be presented in section 4.3.)

This analysis indicates the thermal ion temperature is isotropic or weakly anisotropic throughout the flight. This weak anisotropy matches the prediction calculated from the *Glatthor and Hernández* [1990] results. Inside ArcB ($T$ + 286–337 s), the expected anisotropy is less than 1.01, corresponding to a perpendicular ion temperature of 0.05–0.07 eV. In the DCR poleward of the arc, the expected anisotropy increases to 1.05 at approximately $T$ + 393 s and reaches a maximum value of 1.08 at $T$ + 421 s; in this same region the perpendicular ion temperature ranges from 0.09–0.15 eV. These temperature anisotropies are too weak to generate measurable ion upflow. As a point of comparison, contemporaneous and collocated PFISR data indicate ion temperatures in the range of 0.1–0.2 eV throughout the flight.

Knowing the limits of the DC electric field-driven anisotropy in this portion of the flight, we identify the blue and red traces in Figure 5 (bottom) as the best estimates of the thermal ion upflows and downflows for this period from $T$+286 s onward. In the DCR poleward of the arc ($T$+338–421 s) where the anisotropy is less than 1.1 (see Figure 8), we observe downflows of several hundred m $s^{-1}$. Inside ArcB ($T$ + 286–337 s) where the temperature is approximately isotropic, we observe upflows ranging from a few tens to 300 m $s^{-1}$. Coinciding with the upflows in ArcB are enhanced electron temperature and field-aligned currents, as seen in Figure 2d and 2e. Analysis by *Cohen et al.* [2015] of these observations of enhanced $T_e$ and FAC within ArcB are consistent with models of Type 2 upflow, typically observed above the *F* region density peak. This observed upflow is independent of the ion temperature, which is quite low throughout this region. This case study provides an interesting juxtaposition of heating processes, as we observe frictional processes controlling the ion temperature (typical of a Type 1 upflow event) in the vicinity of ArcB, but because the ions are cold, the ion upflow is attributed to the ambipolar field resulting from the heated electron population, as is typical in a Type 2 upflow event (though we allow for the possibility that ion-neutral collisions may also influence the upflow at these low altitudes).

Within ArcB linear regression analysis indicates a strong positive correlation ($R$ = 0.73) between the parallel flows of the bulk thermal ions ($u_{||}$) and the field-aligned current ($J_z$). This observed relationship reflects the statistical findings of *Kervalishvili and Lühr* [2013] who observed ion upflows that coincide with small-scale

field-aligned currents. This fine-scale observation in the MICA case study shows a correlation between $J_z$ and $u_{\|}$ to the level of local structuring within the arc (tens of kilometers) and not simply a large-scale statistical correlation.

These observations are compared with the multifluid ionospheric model of *Zettergren and Semeter* [2012] in section 4.3. They are also consistent with previous radar and satellite observations of field-aligned ion flows. *Jones et al.* [1988] report nightside EISCAT measurements of ion upflow of 50–90 m s$^{-1}$ at 300 km altitude, and *Semeter et al.* [2003] report upflows of 150 m s$^{-1}$ at this same altitude. *Loranc et al.* [1991] report premidnight auroral zone upflows and downflows measured by the Dynamic Explorer 2 (DE2) satellite, with upflows primarily in the range 100–250 m s$^{-1}$ at altitudes between 216–400 km and downflows consistently smaller than upflows. Downflows below the *F* region peak are quite common due to pressure and gravity forces driving ions downward [*Rishbeth and Garriot*, 1969; *Buchert et al.*, 2004].

Calculation of the in situ observed $\vec{E} \times \vec{B}$ drift velocity in this region indicates plasma is flowing horizontally (perpendicular to $\vec{B}_0$) at an average speed of 133 m s$^{-1}$ with a component poleward from the long axis of the nearly east-west aligned auroral arc. Within the arc, precipitation is heating the electrons, the ions are upwelling, and no ion heating is observed; these observations are consistent with Type 2 upflow (though neutrals may influence the ion dynamics at these low altitudes). Simultaneously, the bulk ion population is $\vec{E}\times\vec{B}$ drifting poleward into the dark downward current region, where the plasma is out of the upflow region, and a combination of collisions and gravity slows the upflow and causes the ions to fall back earthward. Because the payload is near the *F* region peak, we cannot exclude the possibility of altitude dependence for these observed downflowing ions. However, because of the sharp transition from upflow to downflow at the poleward edge of ArcB, we presume the payload is traveling through perpendicularly structured regions of parallel flows.

These falling ions are observed by the MICA payload as downflowing ions poleward of the arc, in agreement with statistical [*Kervalishvili and Lühr*, 2013; *Redmon et al.*, 2010; *Loranc et al.*, 1991; *Wu et al.*, 2000] and remote sensing [*Ogawa et al.*, 2009] results showing downflowing ions measured poleward of upwelling populations. While *Redmon et al.* [2010] use DMSP statistical data to show the boundary between upflows and downflows corresponding to the poleward boundary of the auroral oval, our case study indicates a transition from upflow to downflow at the poleward edge of the discrete arc (equatorward of the poleward boundary of the overall auroral oval, as there are other discrete arcs northward of our in situ observations). Our case study aligns with the statistical study of DE2 observations by *Loranc et al.* [1991] who found discrete regions of upflow and downflow interleaved throughout the auroral zone.

We quantify our observations by calculating several parameters of this plasma circulation example. We measure the width of the heating region by extracting the size of ArcB from the Venetie imager data and calculate the average $\vec{E} \times \vec{B}$ drift velocity $v_{E\times B} = 133$ m s$^{-1}$. Assuming the upflow region extends the full width of ArcB, we determine that the plasma reaches a height of 10–65 km above the payload before falling back toward Earth after exiting the arc. A schematic of this ionospheric circulation is shown in Figure 9.

### 4.2. Processes Influenced by WPI: $T + 163$–$285$ s

Now we turn to the first half of the flight. Referencing Figure 7 for this early interval of the flight, we observe no significant correlation between $T_i$ and $E'^2$, indicating that frictional heating is not the controlling heating mechanism for the thermal ion population. Figure 8 (right) shows time series of $T_e$ (measured by ERPA), $T_{i,\perp}$ (from analysis of HT measurements), and the modeled $O^+$ $T_\perp$ (from the steady state solution to 13-moment energy and pressure tensor equations shown in section 4.1). Inside and in the vicinity of ArcA ($T + 200$–$285$ s), linear regression analysis indicates very little correlation between $T_e$ and $T_i$ ($R = 0.14$), which may be attributed to hysteresis regulating the efficiency of thermal coupling between ions and electrons. The 13-moment calculations show, in particular, that heat exchange between the electrons (which have been heated by precipitation), and the ions does not account for the high ion temperature excursions in the early flight. In this region, linear regression analysis indicates that the correlation between $T_i$ and the logarithm of ELF power (16–80 Hz) is $R = 0.25$, while the correlation between $T_e$ and log ELF power is $R = 0.23$. It appears that modest ion energy input due to wave-particle interactions may be required to produce these ion temperature enhancements. We next examine ion heating possibly driven by WPI observed in the early flight, but further modeling will have to await more detailed simulations capable of accounting for heating of the ions in the presence of collisional effects.

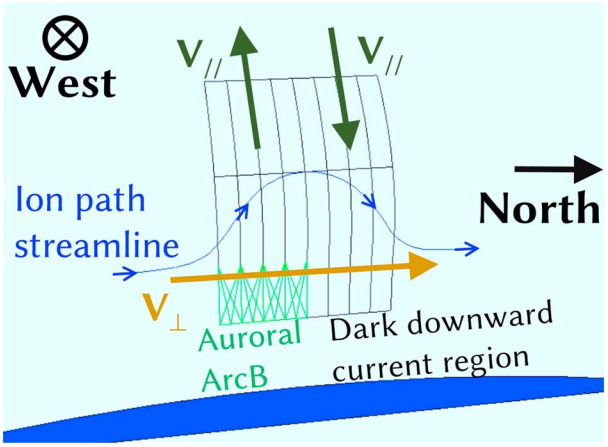


**Figure 9.** Cartoon showing plasma circulation. The ions are $\vec{E} \times \vec{B}$ drifting northward. When these ions pass into ArcB, they remain cold but begin upflowing. MICA observes these upflowing ions inside ArcB ($T$ + 286–337 s). Once these ions exit the arc and thus exit the upflow region, they enter the dark downward current region and fall earthward, which MICA observes as downflows for $T$ + 338–421 s.

In the early flight, MICA observes inflowing DC Poynting flux of several mW m$^{-2}$ (Figure 6) as well as localized increases in the in situ measured ELF power (Figure 10). Near and within ArcA ($T$ + 200–285 s) we observe a weak correlation ($R$ = 0.25) between $T_i$ and the logarithm of the ELF wave power, shown in Figure 10. Bursts of enhanced $T_i$ and ELF power are accompanied by precipitating electrons with energy spectra from 0.5 to 2 keV indicative of Alfvénic activity (these data, from the Bagel instrument, are not shown because the instrument lost power at approximately $T$ + 254 s). Several factors can account for the weak and sporadic correlation between $T_i$ and the ELF wave power. Because the MICA measurements come in the wake of a westward traveling surge, prior heating of the ionospheric plasma due to this energy input likely affects the temperature resulting from a given ELF input. This complicates, to a degree, the interpretation of the $T_i$/ELF correlation. Additionally, the horizontal flow of plasma through a fixed region of heating/precipitation may also contribute to a poor local correlation between the ion temperature and the measured ELF wave power. (It is interesting to note here that apparently equivalent bursts of ELF power in the second half of the flight do not appear to affect $T_i$, with the exception of the aforementioned burst of BBELF at $T$ + 350 s.)

During this first half of the flight, video observations from the Venetie medium-field imager indicate Alfvénic activity in the form of tall rayed auroral structures. Figure 11 shows a snippet from the in situ electric and magnetic field data; during the period $T$ + 200–235 s we see oscillations in the electric and magnetic field data associated with Alfvén waves. We use these measurements to estimate the Alfvén velocity $v_A = \delta E/\delta B \approx 200$ km s$^{-1}$. This corresponds to an Alfvén conductance $\Sigma_A = 0.25$ S which is much smaller than the Pedersen conductance $\Sigma_P = 20$ S (calculated for the MICA case study by *Lynch et al.* [2015]), as is typical for Alfvén waves [*Paschmann et al.*, 2003]. These evidences of Alfvénic activity (an indirect source for ELF WPI)

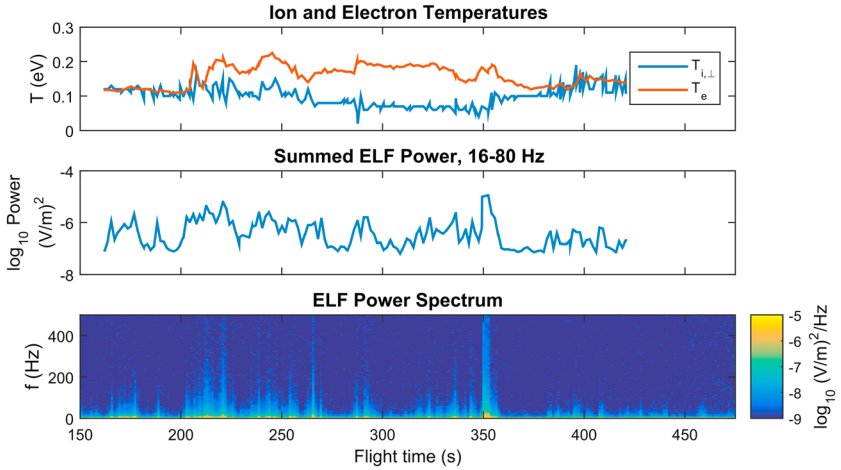


**Figure 10.** Ion temperature and log ELF wave power (16–80 Hz). During the first half of the flight we observe weak and sporadic correlation between the ion temperature and the ELF wave power (correlation coefficient $R$ = 0.25 near and within ArcA, $T$ + 200–285 s). Hysteresis in the wake of the westward traveling surge and the horizontal flow of plasma through fixed heating/precipitation can affect coupling between $T_i$ and ELF wave power and result in a poor local correlation.

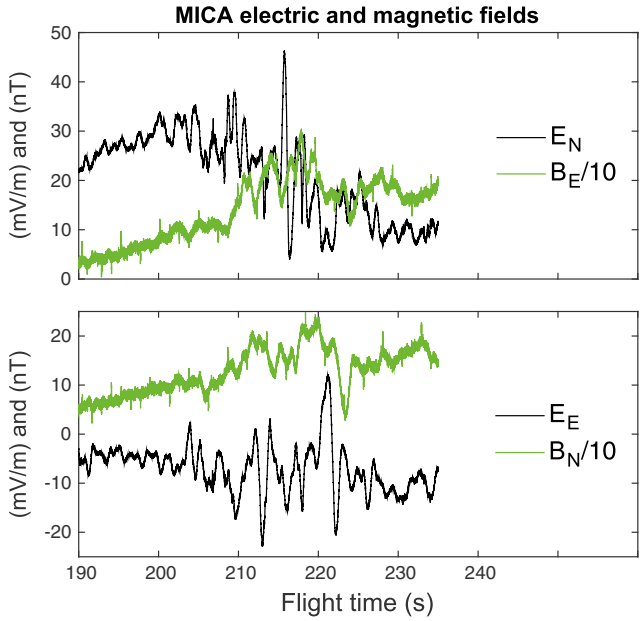


**Figure 11.** In situ electric and magnetic field data. We observe oscillations in the electric field data in the 0.1–10 Hz range typically associated with Alfvén waves. Because these oscillations exist for a small number of cycles and are irregular we cannot extract phasing information. However, we do extract an approximate Alfvén velocity $v_A \approx 200$ km s$^{-1}$.

from a variety of ground-based and in situ observations lead us to consider heating of the bulk thermal ion population by wave-particle interactions.

We can calculate an idealized WPI heating effect ignoring the effects of collisionality and other processes, just to determine whether there is enough ELF wave power to account for the observed ion heating. This idealized WPI heating is calculated from the measured spectral energy density at the ion cyclotron frequency using the quasi-linear technique described by *Chang et al.* [1986]. This simplifying calculation indicates that the ELF-driven WPI alone is sufficient to raise the ion temperature from its origins at the neutral temperature of 0.066 eV to a level of 0.2 eV (above our observations) in the time it would take to move at a constant upward velocity to our observation point. A more rigorous assessment awaits the inclusion of WPI effects in the ionospheric model of *Zettergren and Semeter* [2012], but this rough calculation shows the WPI have the potential to influence the ions here. Heating by WPI is typically in the transverse direction [*Chang and Coppi*, 1981], and therefore, our analysis of the thermal ion data for this interval must account for the possibility of a temperature anisotropy beyond that generated by the DC electric fields.

At these collisional ionospheric altitudes, with observed in situ electric field magnitudes of less than 50 mV m$^{-1}$, the maximum expected temperature anisotropy due to DC electric fields is approximately 1.05, using the analysis described in section 4.1 and shown in Figure 8. When considering the effects of transverse heating by WPI the temperature anisotropy can far exceed this. However, at these altitudes, the temperature anisotropy will be governed by both ion-neutral and ion-ion collisions, which will tend to destroy any large anisotropies [*St-Maurice and Schunk*, 1979].

Figure 5 shows the resulting time series of $T_i$ and $u_{||}$ for temperature anisotropies ranging from 1.0–2.0. Although the anisotropy generated by WPI heating could be higher than 2.0, the resulting $u_{||}$ shown in Figure 5 indicates a reasonable upper limit of 2.0 for the anisotropy, as any larger would result in an unreasonable interpretation of the ion data with downflows in the many hundreds of m s$^{-1}$ at altitudes below 300 km; larger anisotropies also require unreasonably low ion temperatures.

Figure 5 indicates that the parallel bulk ion flow $u_{||}$ is quite sensitive to the inclusion of a temperature anisotropy whereas $T_i$ is mostly unaffected. The possible presence of WPI would result in this temperature anisotropy but could not cause the colocated upflow, as the mirror force is more than an order of magnitude weaker than the gravitational force at these low altitudes and ion energies. We attribute the ion upflow to the

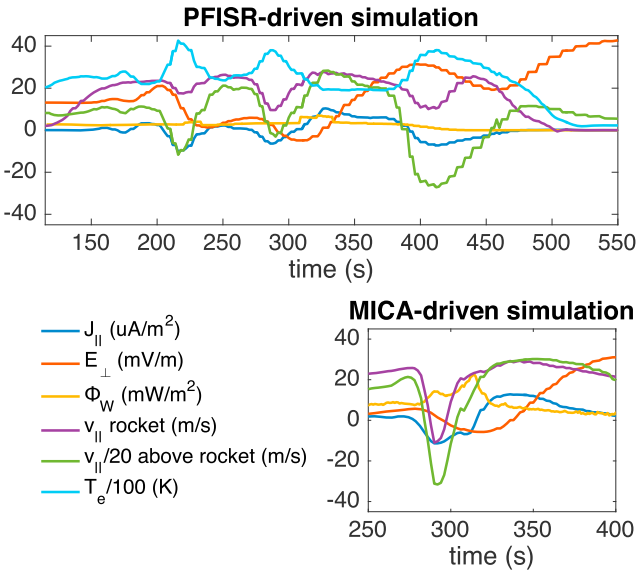


**Figure 12.** Results from two simulations using the ionospheric model of *Zettergren and Semeter* [2012] taken along the MICA trajectory. Model inputs include electric field data $E_{\perp}$ (from (top) PFISR and from (bottom right) MICA COWBOY instrument) and electron energy flux $\Phi_w$ (from (top) Poker Flat all-sky imager and (bottom right) Venetie medium-field imager). Model outputs include current density $J_{||}$ and parallel ion flows $v_{||}$. Figure 12 (bottom right) is the fine-scale, high-resolution simulation that encapsulates the apogee portion of the flight. Figure 12 (top) shows a lower resolution simulation that covers the full rocket trajectory. The model flows are generally downward (positive), although upflows occur at the region of strong precipitation in the fine-scale simulation, matching the upflows observed by the MICA payload within ArcB.

ambipolar electric field generated by the increased electron scale height as the electrons are heated by bursts of precipitation. We also cannot preclude the possibility of neutral upwelling driving the ion upflow through collisional and/or charge exchange processes. This region is typical of Type 2 upflow, but the observations are too low to observe the mirror force acceleration effects associated with electron precipitation and BBELF typical of a Type 2 upflow event. The observations by MICA are the low-altitude signatures in the region in which the upflow is initiated—these signatures are the seeds of ion upflow/outflow.

For this early half of the flight ($T$ + 163–285 s) where WPI are to be considered, an important question arises from this analysis: how do we choose the "correct" level of anisotropy? With the present data set and modeling we can place bounds on the upflow velocities for this portion of the flight but are unable to identify the exact degree of anisotropy. In this region (before $T$ + 286 s), anisotropy values of 1.0–1.5 give upflows at these altitudes, ranging from a few tens to a few hundred m $s^{-1}$, and anisotropy values of 1.5 and 2.0 indicate downflows. These flows are compared to modeling results in section 4.3.

### 4.3. Modeling

Two simulations are conducted using the model of *Zettergren and Semeter* [2012], by constraining the boundary conditions using electric field and precipitation measurements as in *Zettergren et al.* [2014]. Electric field inputs can be either ground-based PFISR measurements or MICA in situ measurements made by the COWBOY instrument. Electron precipitation inputs come from either the all-sky imager at Poker Flat or the medium-field imager at Venetie. In both cases, camera data is converted to electron energy flux.

The first is a fine-scale, high-resolution simulation that uses Venetie medium-field imager data to specify electron precipitation (0.5 s cadence) and MICA DC electric fields as measured by the COWBOY instrument [*Lynch et al.*, 2015]. This simulation encapsulates the apogee portion of the MICA flight. The second, larger-scale simulation has a larger grid that contains the entire rocket trajectory. This simulation uses Poker Flat all-sky camera data (13 s cadence) to specify electron precipitation, and PFISR measurements to specify the electric field inputs. Unlike the previously shown steady state 13-moment model (used to calculate DC electric field-driven anisotropy in section 4.1), this *Zettergren and Semeter* [2012] model includes currents but does not include anisotropy.

Upflows computed by the model depend critically on the time history of the plasma heating processes as well as the electron density time history. Specifically, ion upflow is a fairly slow process that requires several minutes to initiate and propagate to topside ionospheric altitudes [*Zettergren and Semeter*, 2012]. Hence, any comparison of data with modeled ion upflows will be subject to error in time history of model drivers. In particular, the simulations are driven with a static electric field versus L shell profile (measured from the rocket) and likely overemphasize ionospheric heating processes since the electric fields (and currents, to a lesser degree) are fixed and have time to heat the ionosphere and cause upwelling. This overemphasis is apparent in the modeled electron temperatures (not shown) in the fine-scale simulation, which exceed the measured values by a factor of at least 2. The larger-scale simulation, which uses the all-sky camera data to constrain the electron precipitation, has approximately correct electron temperature values.

Figure 12 shows modeled current densities, fields, and field-aligned velocities extracted along the path of MICA. In the model there is a clear correlation between the upward currents and enhancements in upward ion velocity at high altitudes. These are driven, in large part, by high electron temperatures. At the rocket altitudes the flows are generally downward for the large-scale simulations, while for the finer-scale simulation the intense precipitation and strong currents are able to create an ion upflow at the rocket altitudes, as in the data. However, as previously mentioned, the modeled electron temperatures for the fine-scale run greatly exceed those observed via the ERPA instrument on MICA. Hence, we are not able to obtain complete agreement between modeled temperatures and velocities and those seen on MICA. This inconsistency is at least partially due to the lack of knowledge of electric field time history but may also be a consequence of low-altitude transverse ion heating, which is not presently included in this electrostatic model.

## 5. Conclusions

The thermal ion data from the MICA sounding rocket provide a case study of the response of thermal ion kinetic particle distributions in two distinct regions defined by the processes driving the thermal ion behavior. Using a 3-D Maxwellian model to replicate possible measured spectra, we calculate intermediate parameters WAPA and RFA from the model and compare with equivalent parameters calculated from the in situ data. Liouville's theorem and the thin-sheath approximation allow us to couple these measured and modeled intermediate parameters through a forward-modeling technique such that measurements inside the sheath provide information about the state of the plasma outside the sheath.

In the second half of the flight, quasi-static frictional drivers control the ion temperature. We observe a strong positive correlation between $T_i$ and $E'^2$ ($R = 0.78$) indicative of frictional heating. A linear fit indicates a neutral temperature of 770 $\pm$ 230 K and good agreement with theoretical predictions. This strong agreement between theory and data serves as a metric to validate our forward-modeling ion data analysis technique. In this region the anisotropy is expected to be less than 1.10, and we observe upflows as large as 350 m $s^{-1}$ inside ArcB and downflows of several hundreds of m $s^{-1}$ in the poleward downward current region. Within ArcB we observe upflowing ions, enhanced electron temperature and strong FAC, typical of electron precipitation-driven upflow (though we cannot preclude the possibility of neutrals influencing the ion dynamics). Inside this arc the ion temperatures remain cold (independent of the upflow), and we observe a positive localized correlation between the upflow and the FAC ($R = 0.73$).

In the first half of the flight we measure no significant correlation between $T_i$ and $E'^2$. We observe a large inflowing DC Poynting flux, auroral arcs with vertical rayed structure, precipitating electron signatures, and fluctuations in the electric and magnetic fields which are all indicative of Alfvénic activity and the indirect but corresponding effects of heating, possibly by wave-particle interactions. We interpret this transverse heating as a temperature anisotropy in the thermal ion distribution function, with the degree of anisotropy ranging from 1.1–2.0. We observe upflows of several hundred m $s^{-1}$ throughout the entire region, which we show cannot be attributed to the mirror force. We attribute these upflows to the ambipolar electric field generated by the increased electron scale height, and we allow for the possibility of neutral upwelling influencing the bulk ion motion along the magnetic field. We also observe a positive correlation ($R = 0.25$) between $T_i$ and the logarithm of the ELF wave power near and within ArcA. While this does not demonstrate a one-to-one relation between ELF waves and ion heating, the general correspondence between the two in this region suggests that WPI does play a role in generating anisotropy levels that are significantly higher than can be explained by steady state frictional heating.

Our in situ measurements of thermal ion heating and upwelling, at small length scales, are consistent with previous remote sensing and satellite statistical studies on large length scales (hundreds of kilometers) but at altitudes lower than have been previously reported. Additionally, the local ionospheric structure observed by MICA is below the resolution of radar or satellite measurements. Our comparisons with the ionospheric model of *Zettergren and Semeter* [2012] reproduce some of the measured parallel flow structures, including upflow in regions of strong precipitation and downflow in the poleward DCR. Inconsistencies between the data and ionospheric model are partially due to lack of knowledge of the electric field time history, and inconsistencies early in the flight may be a consequence of low-altitude Alfvénic-driven ELF heating, which is not yet accounted for in the model.

As mentioned previously, strong heating by WPI has been observed at altitudes as low as 500 km, but not lower. This is consistent with the fact that the efficiency of a wave heating process would be destroyed by collisions. With regards to gyroresonant wave heating (a likely contributor to transverse energization), it is possible for ions to undergo many uninterrupted gyro-orbits between collisions at altitudes at least a few neutral scale heights above 120 km, where the ion gyrofrequency and collision frequency are approximately equal. This indicates that some level of wave heating is plausible over much of the MICA trajectory (D. Knudsen, personal communication, 2015). This MICA case study has shown the need to consider the effects of WPI at altitudes below 500 km. A more comprehensive study of wave heating in the weakly collisional *F* region is planned for a future study.

The low-altitude observations of the MICA case study will serve to inform future ionospheric observations, modeling, and simulations of, specifically, (a) the need to consider heating by wave-particle interactions at altitudes lower than previously considered viable and (b) the occurrence of structured and localized upflows and downflows on a Type 2 field line before and below where higher-altitude heating processes are expected.

**Acknowledgments**

The MICA analysis is dedicated to the memory of Paul M Kintner, Jr. MICA analysis work at Dartmouth College was funded by NASA grant NNX10AL18G, NASA space grant NNX10AL97H, and by Dartmouth College's Presidential Scholar and Senior Honors Thesis programs. Work at ERAU was funded by NSF grant AGS-1339537, at UAF/GI by NASA grant NNX10AL20G, at UNH by NASA grant NNX10AL17G, and at Cornell by NASA grant NNX10AL16G. Work at UiO has been supported by the ESA PRODEX contract 4200090335 and the Research Council of Norway grant 230996. The MICA team thanks the engineering group at NASA Wallops Flight Facility and NSROC for their hard work and dedication to sounding rocket missions. The MICA project was aided by SRI/PFISR, and by the UAF/GI staff at Poker Flat Research Range. We thank Bryan Wright at ERAU for analysis of the PFISR ion temperature data. The authors thank David Knudsen for his substantive constructive commentary on the manuscript. All data may be requested from the lead author.

## References

Anderson, C., M. Conde, and M. G. McHarg (2012a), Neutral thermospheric dynamics observed with two scanning Doppler imagers: 3. Horizontal wind gradients, *J. Geophys. Res.*, *117*, A05311, doi:10.1029/2011JA017471.

Anderson, C., M. Conde, and M. G. McHarg (2012b), Neutral thermospheric dynamics observed with two scanning Doppler imagers: 1. Monostatic and bistatic winds, *J. Geophys. Res. Space Physics*, *117*, A03304, doi:10.1029/2011JA017041.

André, M., and A. W. Yau (1997), Theories and observations of ion energization and outflow in the high latitude magnetosphere, *Space Sci. Rev.*, *80*, 27–48, doi:10.1023/A:1004921619885.

André, M., H. Koskinen, L. Matson, and R. Erlandson (1988), Local transverse ion energization in and near the polar cusp, *Geophys. Res. Lett.*, *15*(1), 107–110, doi:10.1029/GL015i001p00107.

Arnoldy, R. L., K. A. Lynch, P. M. Kintner, J. Vago, S. Chesney, T. E. Moore, and C. J. Pollock (1992), Bursts of transverse ion acceleration at rocket altitudes, *Geophys. Res. Lett.*, *19*(4), 413–416, doi:10.1029/92GL00091.

Arnoldy, R. L., K. A. Lynch, P. M. Kintner, J. W. Bonnell, T. E. Moore, and C. J. Pollock (1996), SCIFER—Structure of the cleft ion fountain at 1400 km altitude, *Geophys. Res. Lett.*, *23*(14), 1869–1872.

Bekkeng, T. A., K. S. Jacobsen, J. K. Bekkeng, A. Pedersen, T. Lindem, J.-P. Lebreton, and J. I. Moen (2010), Design of a multi-needle Langmuir probe system, *Meas. Sci. Technol.*, *21*, 085903, doi:10.1088/0957-0233/21/8/085903.

Blelly, P. L., D. Alcaydé, and A. P. van Eyken (2010), A new analysis method for determining polar ionosphere and upper atmosphere characteristics from ESR data: Illustration with IPY period, *J. Geophys. Res.*, *115*, A09322, doi:10.1029/2009JA014876.

Brambles, O. J., W. Lotko, B. Zhang, M. Wiltberger, J. Lyon, and R. J. Strangeway (2011), Magnetosphere sawtooth oscillations induced by ionospheric outflow, *Science*, *332*, 1183–1186, doi:10.1126/science.1202869.

Brekke, A., and Y. Kamide (1996), On the relationship between Joule and frictional heating in the polar ionosphere, *J. Atmos. Terr. Phys.*, *58*, 139–143, doi:10.1016/0021-9169(95)00025-9.

Buchert, S. C., Y. Ogawa, R. Fujii, and A. P. van Eyken (2004), Observations of diverging field-aligned ion flow with the ESR, *Ann. Geophys.*, *22*(3), 889–899, doi:10.5194/angeo-22-889-2004.

Burchill, J. K. (2003), High-resolution observations of core and suprathermal ions in the auroral ionosphere: Techniques and results from the GEODESIC sounding rocket, PhD thesis, Univ. of Calgary, Calgary, Canada.

Burchill, J. K., D. J. Knudsen, B. J. J. Bock, R. F. Pfaff, D. D. Wallis, J. H. Clemmons, S. R. Bounds, and H. Stenbaek-Nielsen (2004), Core ion interactions with BB ELF, lower hybrid, and Alfvén waves in the high-latitude topside ionosphere, *J. Geophys. Res.*, *109*, A01219, doi:10.1029/2003JA010073.

Burchill, J. K., D. J. Knudsen, J. H. Clemmons, K. Oksavik, R. F. Pfaff, C. T. Steigies, A. W. Yau, and T. K. Yeoman (2010), Thermal ion upflow in the cusp ionosphere and its dependence on soft electron energy flux, *J. Geophys. Res.*, *115*, A05206, doi:10.1029/2009JA015006.

Carlson, C. W., D. W. Curtis, G. Paschmann, and W. Michael (1983), An instrument for rapidly measuring plasma distribution functions with high resolution, *Adv. Space Res.*, *2*(7), 67–70, doi:10.1016/0273-1177(82)90151-X.

Chang, T., and B. Coppi (1981), Lower hybrid acceleration and ion evolution in the suprauroral region, *Geophys. Res. Lett.*, *8*(12), 1253–1256, doi:10.1029/GL008i012p01253.

Chang, T., G. B. Crew, N. Hershkowitz, J. R. Jasperse, J. M. Retterer, and J. D. Winningham (1986), Transverse acceleration of oxygen ions by electromagnetic ion cyclotron resonance with broad band left-hand polarized waves, *Geophys. Res. Lett.*, *13*(7), 636–639, doi:10.1029/GL013i007p00636.

Chaston, C. C., J. W. Bonnell, L. M. Peticolas, C. W. Carlson, and J. P. McFadden (2002), Driven Alfven waves and electron acceleration: A FAST case study, *Geophys. Res. Lett.*, *29*(11), 1535, doi:10.1029/2001GL013842.

Chaston, C. C., J. W. Bonnell, C. W. Carlson, J. P. McFadden, R. E. Ergun, R. J. Strangeway, and E. J. Lund (2004), Auroral ion acceleration in dispersive Alfvén waves, *J. Geophys. Res.*, *109*, A04205, doi:10.1029/2003JA010053.

Cohen, I. J., M. R. Lessard, R. H. Varney, K. A. Lynch, K. Oksavik, and M. Zettergren (2015), Ion upflow dependence on ionospheric density and solar photoionization, *J. Geophys. Res. Space Physics*, *120*, 10,039–10,052, doi:10.1002/2015JA021523.

Conde, M., and R. W. Smith (1998), Spatial structure in the thermospheric horizontal wind above Poker Flat, Alaska, during solar minimum, *J. Geophys. Res.*, *103*, 9449–9471, doi:10.1029/97JA03331.

Demars, H. G., and R. W. Schunk (2007), Thermospheric response to ion heating in the dayside cusp, *J. Atmos. Sol. Terr. Phys.*, *69*(6), 649–660, doi:10.1016/j.jastp.2006.11.002.

Dombeck, J., C. Cattell, J. R. Wygant, A. Keiling, and J. Scudder (2005), Alfvén waves and Poynting flux observed simultaneously by Polar and FAST in the plasma sheet boundary layer, *J. Geophys. Res.*, *110*, A12S90, doi:10.1029/2005JA011269.

Forme, F. R. E., D. Fontaine, and J. E. Wahlund (1995), Two different types of enhanced ion acoustic fluctuations observed in the upper ionosphere, *J. Geophys. Res.*, *100*, 14,625–14,636, doi:10.1029/94JA01093.

Frederick-Frost, K. M., and K. A. Lynch (2007), Low energy stable plasma calibration facility, *Rev. Sci. Instrum.*, *78*, 075113, doi:10.1063/1.2756996.

Frederick-Frost, K. M., K. A. Lynch, P. M. Kintner, E. Klatt, D. Lorentzen, J. Moen, Y. Ogawa, and M. Widholm (2007), SERSIO: Svalbard EISCAT rocket study of ion outflows, *J. Geophys. Res.*, *112*, A08307, doi:10.1029/2006JA011942.

Gayetsky, L. E., and K. A. Lynch (2011), Note: Flowing ion population from a resonance cavity source, *Rev. Sci. Instrum.*, *82*(4), 046112, doi:10.1063/1.3584969.

Glatthor, N., and R. Hernández (1990), Temperature anisotropy of drifting ions in the auroral F-region, observed by EISCAT, *J. Atmos. Terr. Phys.*, *52*(1988), 545–560, doi:10.1016/0021-9169(90)90052-O.

Heelis, R. A., and W. B. Hanson (1998), Measurements of thermal ion drift velocity and temperature using planar sensors, in *Measurement Techniques in Space Plasmas: Particles*, edited by R. F. Pfaff, J. E. Borovsky, and D. T. Young, pp. 61–71, AGU, Washington, D. C., doi:10.1029/GM102p0061.

Hoffman, J. H. (1970), Studies of the composition of the ionosphere with a magnetic deflection mass spectrometer, *Int. J. Mass Spectrom. Ion Phys.*, *4*, 315–322, doi:10.1016/0020-7381(70)85047-1.

Horak, P. (2014), Attitude estimation for rocket-borne sensorcraft, Senior honors thesis, Dartmouth College, Hanover, N. H.

Horwitz, J. L., and T. E. Moore (1997), Four contemporary issues concerning ionospheric plasma flow to the magnetosphere, *Space Sci. Rev.*, *80*, 46–79, doi:10.1023/A:1004973603955.

Jacobsen, K. S., A. Pedersen, J. I. Moen, and T. A. Bekkeng (2010), A new Langmuir probe concept for rapid sampling of space plasma electron density, *Meas. Sci. Technol.*, *21*, 085902, doi:10.1088/0957-0233/21/8/085902.

Jones, G. O. L., P. J. S. Williams, K. J. Winser, M. Lockwood, and K. Suvanto (1988), Large plasma velocities along the magnetic field line in the auroral zone, *Nature*, *336*, 403–405, doi:10.1038/336231a0.

Kelley, M. C. (2009), *The Earth's Ionosphere: Plasma Physics and Electrodynamics*, 2nd ed., Elsevier Sci., London.

Kervalishvili, G. N., and H. Lühr (2013), The relationship of thermospheric density anomaly with electron temperature, small-scale FAC, and ion up-flow in the cusp region, as observed by CHAMP and DMSP satellites, *Ann. Geophys.*, *31*, 541–554, doi:10.5194/angeo-31-541-2013.

Kintner, P. M., J. W. Bonnell, R. L. Arnoldy, K. A. Lynch, C. J. Pollock, and T. E. Moore (1996), SCIFER-Transverse ion acceleration and plasma waves, *Geophys. Res. Lett.*, *23*(14), 1873–1876, doi:10.1029/96GL01863.

Knudsen, D. J., B. A. Whalen, A. W. Yau, M. J. Greffen, A. I. Eriksson, N. Lloyd, M. H. Boehm, J. Clemmons, and L. Blomberg (1994), Sub-kilometer thermal plasma structure near 1750-km altitude in the polar cusp cleft, *Geophys. Res. Lett.*, *21*(17), 1907–1910, doi:10.1029/94GL00887.

Knudsen, D. J., T. D. Phan, M. D. Gladders, and M. J. Greffen (1998a), Thermal electron temperature measurements from the Freja cold plasma analyzer, in *Measurement Techniques in Space Plasmas: Particles*, edited by R. F. Pfaff, J. E. Borovsky, and D. T. Young, pp. 91–96, AGU, Washington, D. C., doi:10.1029/GM102p0091.

Knudsen, D. J., J. H. Clemmons, and J. E. Wahlund (1998b), Correlation between core ion energization, suprathermal electron bursts, and broadband ELF plasma waves, *J. Geophys. Res.*, *103*(A3), 4171–4186, doi:10.1029/97JA00696.

Knudsen, D. J., J. K. Burchill, K. Berg, T. Cameron, G. A. Enno, C. G. Marcellus, E. P. King, I. Wevers, and R. A. King (2003), A low-energy charged particle distribution imager with a compact sensor for space applications, *Rev. Sci. Instrum.*, *74*(1), 202–211, doi:10.1063/1.1525869.

Koepke, M. E., M. W. Zintl, and T. N. Good (1998), An effect of neutral collisions on the excitation threshold of electrostatic ion-cyclotron waves, *Geophys. Res. Lett.*, *25*(16), 3095–3098, doi:10.1029/98GL02331.

Kronberg, E. A., et al. (2014), Circulation of heavy ions and their dynamical effects in the magnetosphere: Recent observations and models, *Space Sci. Rev.*, *184*, 173–235, doi:10.1007/s11214-014-0104-0.

Lessard, M. R., E. A. Lindgren, M. J. Engebretson, and C. Weaver (2015), Solar cycle dependence of ion cyclotron wave frequencies, *J. Geophys. Res. Space Physics*, *120*, 4711–4718, doi:10.1002/2014JA020791.

Li, X., and M. Temerin (1993), Ponderomotive effects on ion acceleration in the auroral zone, *Geophys. Res. Lett.*, *20*(1), 12,151–12,161, doi:10.1029/95JA00175.

Loranc, M., J.-P. St.-Maurice, W. B. Hanson, and R. A. Heelis (1991), A morphological study of vertical ionospheric flows in the high-latitude F region, *J. Geophys. Res.*, *96*, 3627–3646, doi:10.1029/90JA02242.

Lühr, H., M. Rother, W. Köhler, P. Ritter, and L. Grunwaldt (2004), Thermospheric up-welling in the cusp region: Evidence from CHAMP observations, *Geophys. Res. Lett.*, *31*, L06805, doi:10.1029/2003GL019314.

Lundberg, E. T., P. M. Kintner, S. P. Powell, and K. A. Lynch (2012a), Multipayload interferometric wave vector determination of auroral hiss, *J. Geophys. Res.*, *117*, A02306, doi:10.1029/2011JA017037.

Lundberg, E. T., P. M. Kintner, K. A. Lynch, and M. R. Mella (2012b), Multi-payload measurement of transverse velocity shears in the topside ionosphere, *Geophys. Res. Lett.*, *39*, L01107, doi:10.1029/2011GL050018.

Lynch, K. A., J. L. Semeter, M. Zettergren, P. Kintner, R. L. Arnoldy, E. Klatt, J. Labelle, and R. G. Michell (2007), Auroral ion outflow: Low altitude energization, *Ann. Geophys.*, *25*, 1967–1977.

Lynch, K. A., et al. (2015), MICA sounding rocket observations of conductivity-gradient generated auroral ionospheric responses: Small-scale structure with large-scale drivers, *J. Geophys. Res. Space Physics*, *120*, 9661–9682, doi:10.1002/2014JA020860.

Lysak, R. L. (1986), Ion acceleration by wave-particle interaction, in *Ion Acceleration in the Magnetosphere and Ionosphere*, edited by T. Chang et al., pp. 261–270, AGU, Washington, D. C., doi:10.1029/GM038p0261.

Marklund, G. T. (2009), Electric fields and plasma processes in the auroral downward current region, below, within, and above the acceleration region, *Space Sci. Rev.*, *142*, 1–21, doi:10.1007/s11214-008-9373-9.

Moen, J., K. Oksavik, and H. C. Carlson (2004), On the relationship between ion upflow events and cusp auroral transients, *Geophys. Res. Lett.*, *31*, L11808, doi:10.1029/2004GL020129.

Moen, J., K. Oksavik, T. Abe, M. Lester, Y. Saito, T. A. Bekkeng, and K. S. Jacobsen (2012), First in-situ measurements of HF radar echoing targets, *Geophys. Res. Lett.*, *39*, L07104, doi:10.1029/2012GL051407.

Moore, T. E., C. J. Pollock, and D. T. Young (1998), Kinetic core plasma diagnostics, in *Measurement Techniques in Space Plasmas: Particles*, edited by R. F. Pfaff, J. E. Borovsky, and D. T. Young, pp. 105–123, AGU, Washington, D. C., doi:10.1029/GM102p0105.

Nilsson, H., M. Waara, S. Arvelius, O. Marghitu, M. Bouhram, Y. Hobara, M. Yamauchi, and R. Lundin (2006), Characteristics of high altitude oxygen ion energization and outflow as observed by Cluster: A statistical study, *Ann. Geophys.*, *24*(3), 1099–1112, doi:10.5194/angeo-24-1099-2006.

Ogawa, Y., S. C. Buchert, R. Fujii, S. Nozawa, and A. P. van Eyken (2009), Characteristics of ion upflow and downflow observed with the European Incoherent Scatter Svalbard radar, *J. Geophys. Res.*, *114*, A05305, doi:10.1029/2008JA013817.

Paschmann, G., S. Haaland, and R. Treumann (Eds.) (2003), *Auroral Plasma Physics*, Springer, Netherlands, doi:10.1007/978-94-007-1086-3.

Perraut, S., N. Bjørna, A. Brekke, M. Baron, W. Kofman, C. Lathuillière, and G. Lejeune (1984), Experimental evidence of non-isotropic temperature distributions of ions observed by EISCAT in the auroral F-region, *Geophys. Res. Lett.*, *11*(5), 519–522, doi:10.1029/GL011i005p00519.

Powell, S. P., E. M. Klatt, and P. M. Kintner (2002), Plasma wave interferometry using GPS positioning and timing on a formation of three sub-orbital payloads, paper presented at 15th International Technical Meeting of the Satellite Division of The Inst. of Navigation (ION GPS 2002), pp. 145–154, Portland, 24–27 Sept.

Redmon, R. J., W. K. Peterson, L. Andersson, E. A. Kihn, W. F. Denig, M. Hairston, and R. Coley (2010), Vertical thermal O+ flows at 850 km in dynamic auroral boundary coordinates, *J. Geophys. Res.*, *115*, A00J08, doi:10.1029/2010JA015589.

Rees, M. H., and D. Luckey (1974), Auroral electron energy derived from ratio of spectroscopic emissions 1. Model computations, *J. Geophys. Res.*, *79*(34), 5181–5186, doi:10.1029/JA079i034p05181.

Reiff, P. H. (1984), Models of auroral-zone conductances, in *Magnetospheric Currents*, vol. 28, edited by T. A. Potemra, pp. 180–191, AGU, Washington, D. C., doi:10.1029/GM028p0180.

Rishbeth, H., and O. K. Garriot (1969), *Introduction to Ionospheric Physics*, Acad. Press, New York.

Sadler, F. B., M. Lessard, E. Lund, A. Otto, and H. Lühr (2012), Auroral precipitation/ion upwelling as a driver of neutral density enhancement in the cusp, *J. Atmos. Sol. Terr. Phys.*, *87–88*, 82–90, doi:10.1016/j.jastp.2012.03.003.

Schlegel, K., H. Lühr, J.-P. St.-Maurice, G. Crowley, and C. Hackert (2005), Thermospheric density structures over the polar regions observed with CHAMP, *Ann. Geophys.*, *23*(5), 1659–1672, doi:10.5194/angeo-23-1659-2005.

Schunk, R. W. (1977), Mathematical structure of transport equations for multispecies flows, *Rev. Geophys.*, *15*(4), 429–445, doi:10.1029/RG015i004p00429.

Schunk, R. W., and A. Nagy (2009), *Ionospheres: Physics, Plasma Physics, and Chemistry*, 2nd ed., Cambridge Univ. Press, Cambridge, U. K.

Semeter, J., C. J. Heinselman, J. P. Thayer, R. A. Doe, and H. U. Frey (2003), Ion upflow enhanced by drifting F-region plasma structure along the nightside polar cap, *Geophys. Res. Lett.*, *30*(22), 2139, doi:10.1029/2003GL017747.

Seo, Y., J. L. Horwitz, and R. Caton (1997), Statistical relationships between high-latitude ionospheric F region/topside upflows and their drivers: DE 2 observations, *J. Geophys. Res.*, *102*, 7493–7500, doi:10.1029/97JA00151.

Seyler, C. E., and K. Liu (2007), Particle energization by oblique inertial Alfvén waves in the auroral region, *J. Geophys. Res.*, *112*, A09302, doi:10.1029/2007JA012412.

Seyler, C. E., A. E. Clark, J. Bonnell, and J.-E. Wahlund (1998), Electrostatic broadband ELF wave emission by Alfvén wave breaking, *J. Geophys. Res.*, *103*(A4), 7027–7041, doi:10.1029/97JA02297.

Shelley, E. G., R. G. Johnson, and R. D. Sharp (1972), Satellite observations of energetic heavy ions during a geomagnetic storm, *J. Geophys. Res.*, *77*(31), 6104–6110, doi:10.1029/JA077i031p06104.

Siddiqui, M. U., L. E. Gayetsky, M. R. Mella, K. A. Lynch, and M. R. Lessard (2011), A laboratory experiment to examine the effect of auroral beams on spacecraft charging in the ionosphere, *Phys. Plasmas*, *18*, 092905, doi:10.1063/1.3640512.

Singh, N., and R. W. Schunk (1984), Energization of ions in the auroral plasma by broadband waves: Generation of ion conics, *J. Geophys. Res.*, *89*, 5538–5546, doi:10.1029/JA089iA07p05538.

Singh, N., G. Khazanov, and A. Mukhter (2007), Electrostatic wave generation and transverse ion acceleration by Alfvén wave components of broadband extremely low frequency turbulence, *J. Geophys. Res.*, *112*, A06210, doi:10.1029/2006JA011933.

Skjæveland, Å., J. I. Moen, and H. C. Carlson (2011), On the relationship between flux transfer events, temperature enhancements and ion upflow events in the cusp ionosphere, *J. Geophys. Res.*, *116*, A10305, doi:10.1029/2011JA016480.

St-Maurice, J.-P., and R. W. Schunk (1979), Ion velocity distributions in the high-latitude ionosphere, *Rev. Geophys.*, *17*(1), 99–134, doi:10.1029/RG017i001p00099.

Stasiewicz, K., P. Bellan, C. Chaston, C. Kletzing, R. Lysak, J. Maggs, O. Pokhotelov, C. Seyler, P. Shukla, L. Stenflo, and A. Streltsov (2000), Small scale Alfvénic structure in the aurora, *Space Sci. Rev.*, *92*, 423–533, doi:10.1023/A:1005207202143.

Strangeway, R. J., R. E. Ergun, Y.-J. Su, C. W. Carlson, and R. C. Elphic (2005), Factors controlling ionospheric outflows as observed at intermediate altitudes, *J. Geophys. Res.*, *110*, A03221, doi:10.1029/2004JA010829.

Strickland, D. J., J. H. Hecht, A. B. Christensen, and R. R. Meier (1989), Deducing composition and incident electron spectra from ground-based auroral optical measurements: Variations in oxygen density, *J. Geophys. Res.*, *94*(A10), 13,553–13,563, doi:10.1029/JA094iA10p13553.

Vasyliunas, V. M., and P. Song (2005), Meaning of ionospheric Joule heating, *J. Geophys. Res.*, *110*, A02301, doi:10.1029/2004JA010615.

Wahlund, J. E., and H. J. Opgenoorth (1989), EISCAT observations of strong ion outflows from the F-region ionosphere during auroral activity: Preliminary results, *Geophys. Res. Lett.*, *16*(7), 727–730, doi:10.1029/GL016i007p00727.

Wahlund, J. E., H. J. Opgenoorth, I. Häggström, K. J. Winser, and G. O. L. Jones (1992), EISCAT observations of topside ionospheric ion outflows during auroral activity: Revisited, *J. Geophys. Res.*, *97*, 3019–3037.

Whalen, B. A., W. Bernstein, and P. W. Daly (1978), Low altitude acceleration of ionospheric ions, *Geophys. Res. Lett.*, *5*(1), 55–58, doi:10.1029/GL005i001p00055.

Whitteker, J. (1977), The transient response of the topside ionosphere to precipitation, *Planet. Space Sci.*, *25*(8), 773–786, doi:10.1016/0032-0633(77)90129-5.

Wu, X., J. L. Horwitz, and Y. Seo (2000), Statistical analysis of F region and topside ionospheric ion field-aligned flows at high latitudes, *J. Geophys. Res.*, *105*, 2477–2494, doi:10.1029/1999JA900437.

Wygant, J. R., A. Keiling, C. A. Cattell, M. Johnson, R. L. Lysak, M. Temerin, F. S. Mozer, C. A. Kletzing, J. D. Scudder, and W. Peterson (2000), Polar spacecraft based comparisons of intense electric fields and Poynting flux near and within the plasma sheet-tail lobe boundary to UVI images: An energy source for the aurora, *J. Geophys. Res.*, *105*, 675–692, doi:10.1029/1999JA900500.

Yau, A. W., B. A. Whalen, A. G. McNamara, P. J. Kellogg, and W. Bernstein (1983), Particle and wave observations of low-altitude ionospheric ion acceleration events, *J. Geophys. Res.*, *88*, 341–355, doi:10.1029/JA088iA01p00341.

Young, D. T., S. J. Bame, M. F. Thomsen, R. H. Martin, J. L. Burch, J. A. Marshall, and B. Reinhard (1988), 2Π-radian field-of-view toroidal electrostatic analyzer, *Rev. Sci. Instrum.*, *59*(5), 743–751, doi:10.1063/1.1139821.

Zettergren, M., and J. Semeter (2012), Ionospheric plasma transport and loss in auroral downward current regions, *J. Geophys. Res.*, *117*, A06306, doi:10.1029/2012JA017637.

Zettergren, M., J. Semeter, B. Burnett, W. Oliver, C. Heinselman, P. L. Blelly, and M. Diaz (2010), Dynamic variability in F-region ionospheric composition at auroral arc boundaries, *Ann. Geophys.*, *28*, 651–664, doi:10.5194/angeo-28-651-2010.

Zettergren, M., J. Semeter, C. Heinselman, and M. Diaz (2011), Incoherent scatter radar estimation of F region ionospheric composition during frictional heating events, *J. Geophys. Res.*, *116*, A01318, doi:10.1029/2010JA016035.

Zettergren, M., K. A. Lynch, D. Hampton, M. Nicolls, B. Wright, M. Conde, J. Moen, M. Lessard, R. Miceli, and S. Powell (2014), Auroral ionospheric F region density cavity formation and evolution: MICA campaign results, *J. Geophys. Res. Space Physics*, *119*, 3162–3178, doi:10.1002/2013JA019583.